nature communications

Article

https://doi.org/10.1038/s41467-024-51016-2

Mitochondrial network reorganization and transient expansion during oligodendrocyte generation

Received: 27 November 2023

Accepted: 24 July 2024

Published online: 14 August 2024

Check for updates

Xhoela Bame[1] & Robert A. Hill[1]

Oligodendrocyte precursor cells (OPCs) give rise to myelinating oligodendrocytes of the brain. This process persists throughout life and is essential for recovery from neurodegeneration. To better understand the cellular checkpoints that occur during oligodendrogenesis, we determined the mitochondrial distribution and morphometrics across the oligodendrocyte lineage in mouse and human cerebral cortex. During oligodendrocyte generation, mitochondrial content expands concurrently with a change in subcellular partitioning towards the distal processes. These changes are followed by an abrupt loss of mitochondria in the oligodendrocyte processes and myelin, coinciding with sheath compaction. This reorganization and extensive expansion and depletion take 3 days. Oligodendrocyte mitochondria are stationary over days while OPC mitochondrial motility is modulated by animal arousal state within minutes. Aged OPCs also display decreased mitochondrial size, volume fraction, and motility. Thus, mitochondrial dynamics are linked to oligodendrocyte generation, dynamically modified by their local microenvironment, and altered in the aging brain.

Insulating, lipid-rich myelin sheaths enwrap axons to accelerate electrical transmission and provide trophic support to neurons[1,2]. The myelin of the central nervous system is synthesized and maintained by oligodendrocytes which derive from a resident population of oligodendrocyte precursor cells (OPCs). Oligodendrocyte generation persists throughout life, holding important roles for plasticity, cognition, and myelin replacement in neurodegenerative pathologies[2–4]. The developmental stages of oligodendrocytes consist of migration and proliferation of OPCs, differentiation, and maturation into myelinating oligodendrocytes[5–7]. Several intrinsic and extrinsic cues, involving transcription and growth factors, axon diameter, and neuronal activity can modulate each of these stages[8–14]. However, the precise mechanisms that guide OPCs to differentiate or undergo cell death are not well defined. To better understand this process, the physiological and subcellular events that occur within these cells in their native environment must be determined.

Mitochondrial activity drives the differentiation, maturation, and cell death of many cell types throughout the body[15–24]. Genes linked to these mitochondrial dynamics vary across the oligodendrocyte lineage[25–27] suggesting that mitochondrial activity could be correlated with fate decisions in this lineage. This is supported by changes in mitochondria during the differentiation of cultured oligodendrocytes[28] along with the association of mitochondria-regulated signaling pathways in modulating OPC survival and myelination[29,30]. Moreover, mitochondrial motility in oligodendrocytes appears low[31,32] but whether the same dynamics apply to OPCs has not been reported. Finally, disrupted mitochondrial function has been associated with aging and neurodegeneration[33,34]. Indeed, aged OPCs, characterized by their reduced potential to differentiate, exhibit hallmarks of mitochondrial dysfunction, and restoring mitochondrial function in these cells can partially restore their ability to differentiate[35].

These observations position mitochondria as multifunctional, plastic organelles with the potential to regulate the fate of OPCs. However, there has never been a systematic analysis of mitochondrial dynamics as OPCs are differentiating or dying. Here, we used a

[1]Department of Biological Sciences, Dartmouth College, Hanover, NH, USA. e-mail: robert.hill@dartmouth.edu

combination of intravital fluorescence and label-free optical imaging to determine the mitochondrial dynamics during these fate decisions in the live intact mouse brain. This was coupled with ultrastructural 3-dimensional analysis of mitochondrial morphometrics in human tissue. Mitochondrial content changed drastically during oligodendrocyte generation with mature oligodendrocytes exhibiting the lowest mitochondrial content out of all stages. Mitochondrial morphology transitioned from more elongated in OPCs to punctate in mature oligodendrocytes. Longitudinal imaging as an OPC transitioned into a myelinating oligodendrocyte revealed a migratory pattern of mitochondria out of the soma and into the processes and the newly formed myelin sheaths. This was followed by an abrupt mitochondrial loss in the distal cell processes and a surge of mitochondria in the soma as the oligodendrocyte matured and the myelin sheaths compacted. Once the oligodendrocytes matured, their mitochondria were remarkably stable over days. In contrast, OPC mitochondria were dynamic and continuously moved throughout the cell. This motility was affected by the animal arousal state as anesthesia and sedation decreased mitochondrial motility. Lastly, alterations in OPC mitochondrial volume fraction, size, and motility were found in aged animals. These results reveal the spatiotemporal dynamics of mitochondria at different fates and ages of OPCs and uncover pathways that impact these dynamics in the live brain.

Results

Labeling and intravital imaging of mitochondria in the oligodendrocyte lineage

Mitochondria are multifunctional organelles known to regulate cell fate but their involvement with oligodendrocyte generation has never been characterized in the live intact brain. To enable visualization of mitochondria specifically in the oligodendrocyte lineage, we generated a triple transgenic mouse line, *Cspg4*-creER: Ai9: PhAM, that has mitochondrial and cell cytoplasmic reporters (respectively, mito-Dendra2 and cyto-tdTomato) in chondroitin sulfate proteoglycan 4 (*Cspg4*)-expressing cells after tamoxifen-inducible Cre recombination (Fig. 1a and Supplementary Fig. 1). To have sparse labeling while also capturing cells at different stages of differentiation, a low dose of tamoxifen was injected on postnatal day (P) 25 to induce Cre recombination. Intravital imaging over the somatosensory cortex was done 3 weeks later (Supplementary Fig. 1a). Thus, during imaging, there was a mixture of cells at the OPC stage, cells actively differentiating, and cells that had differentiated into mature, myelinating oligodendrocytes. To determine the efficiency of mitochondrial labeling in recombined cells, we immunostained tissue sections from these mice for TOM20, a mitochondrial outer membrane protein, and quantified the presence of mito-Dendra2 in TOM20-labeled mitochondria. This analysis revealed a nearly complete coincidence between the two (99.33%; quantification from 150 mitochondrial networks from 30 cells of the oligodendrocyte lineage, see methods), indicating that most, if not all, mitochondria were labeled within the imaged cells (Supplementary Fig. 2).

To distinguish and classify the different cell stages across the lineage, we first used a combination of cell morphology and Spectral Confocal Reflectance (SCoRe) microscopy, a technique that enables label-free visualization of reflective, compact, myelin sheaths[36–38]. OPCs were identified as having no cellular processes that could be identified as sheaths and thus did not associate with any SCoRe signal (Fig. 1b). To separate newly formed and mature oligodendrocytes, we quantified the SCoRe to tdTomato ratio for a subset of sheaths attached to identified cells (Fig. 1b, c). This analysis revealed a clear separation of the two groups with the newly formed sheaths from the new oligodendrocytes showing little to no SCoRe signal (range 0 to 8.8%) and the sheaths from the mature oligodendrocytes having a more complete SCoRe coverage (range 47.2 to 93.3%) that scaled with their compaction, and therefore maturation. We further characterized the cells from these three stages with respect to cell volume, as well as process length (+sheaths when present), and density. The newly formed oligodendrocytes showed the highest total cell and soma volume while the total process length (+sheaths when present) was conserved between all three stages (Fig. 1d). The OPCs, in turn, had the greatest total number of branches (Fig. 1d). Although the newly formed and mature oligodendrocytes had, on average, a similar number of sheaths, the average length of the sheaths coming from mature oligodendrocytes was greater (Fig. 1e).

Mitochondrial morphology and subcellular localization differ across the oligodendrocyte lineage

To determine mitochondrial location, content, and shape across the oligodendrocyte lineage we created 3-dimensional segmentations of single cells and their mitochondria (Fig. 2a, Supplementary Fig. 3). We traced different cellular compartments: soma, processes (primary, secondary, tertiary+), and myelin sheaths along with their mitochondria. We then quantified the following at each stage: 1) mitochondrial volume fraction determined as the ratio of the total volume of mitochondria over the total volume of the whole cell or the cell compartment they occupy, 2) mitochondrial density determined as the number of mitochondria per 100 μm, 3) total mitochondria number, and 4) average mitochondrial length.

Total mitochondrial volume fraction was the lowest in the mature oligodendrocytes while the newly formed oligodendrocytes had the highest total number of mitochondria per cell (excluding the soma due to difficulties in distinguishing individual mitochondrial networks) (Fig. 2b). The mitochondrial volume fraction in the soma, however, was not significantly different between the three stages although the group of newly formed oligodendrocytes spanned a wider range of values (Fig. 2c). Additionally, the processes of newly formed oligodendrocytes had the highest volume fraction and density of mitochondria (Fig. 2d and Supplementary Fig. 3d). The shape of mitochondria in the processes changed from more elongated in OPCs to shorter and punctate in the mature oligodendrocytes (Fig. 2d, Supplementary Fig. 3d, and Supplementary Fig. 4b). Moreover, the sheaths of the newly formed oligodendrocytes had higher mitochondrial volume fraction, density, and length compared to compact sheaths from mature oligodendrocytes (Fig. 2e), which also corresponded to differences in sheath mitochondrial circularity and aspect ratio between newly formed and mature oligodendrocytes (Supplementary Fig. 4c). Finally, correlating the mitochondrial volume fraction in the sheaths to the SCoRe coverage revealed that sheath compaction corresponded to decreased mitochondrial content (Fig. 2f).

To determine if the differences in mitochondrial distribution across the oligodendrocyte lineage based on our morphological criteria aligned with the cell stage-specific markers in fixed tissue, we immunostained for platelet-derived growth factor receptor alpha (PDGFRA), a marker of OPCs, breast carcinoma amplified sequence 1 (BCAS1), a marker of differentiating and newly formed oligodendrocytes, carbonic anhydrase II (CAII), a marker of mature oligodendrocytes, and myelin basic protein (MBP) a marker of compact myelin sheaths. CAII-labeled mature oligodendrocytes had the highest mitochondrial content in the soma and the lowest in the processes compared to PDGFRA-labeled OPCs or BCAS1-labeled differentiating and newly formed oligodendrocytes (Fig. 3b, Supplementary Fig. 5).

Analysis of mitochondrial distribution in the sheaths revealed that newly formed sheaths that extended from BCAS1-labeled cells but lacked MBP labeling were more likely to have at least 1 mitochondrion compared to BCAS1 and MBP dual-labeled sheaths (Fig. 3c, d). In addition, only ~24% of the CAII-labeled mature sheaths contained at least 1 mitochondrion along their length (Supplementary Fig. 6), similar to 21% of the sheaths attached to mature oligodendrocytes classified via SCoRe labeling (Fig. 2e).

https://doi.org/10.1038/s41467-024-51016-2

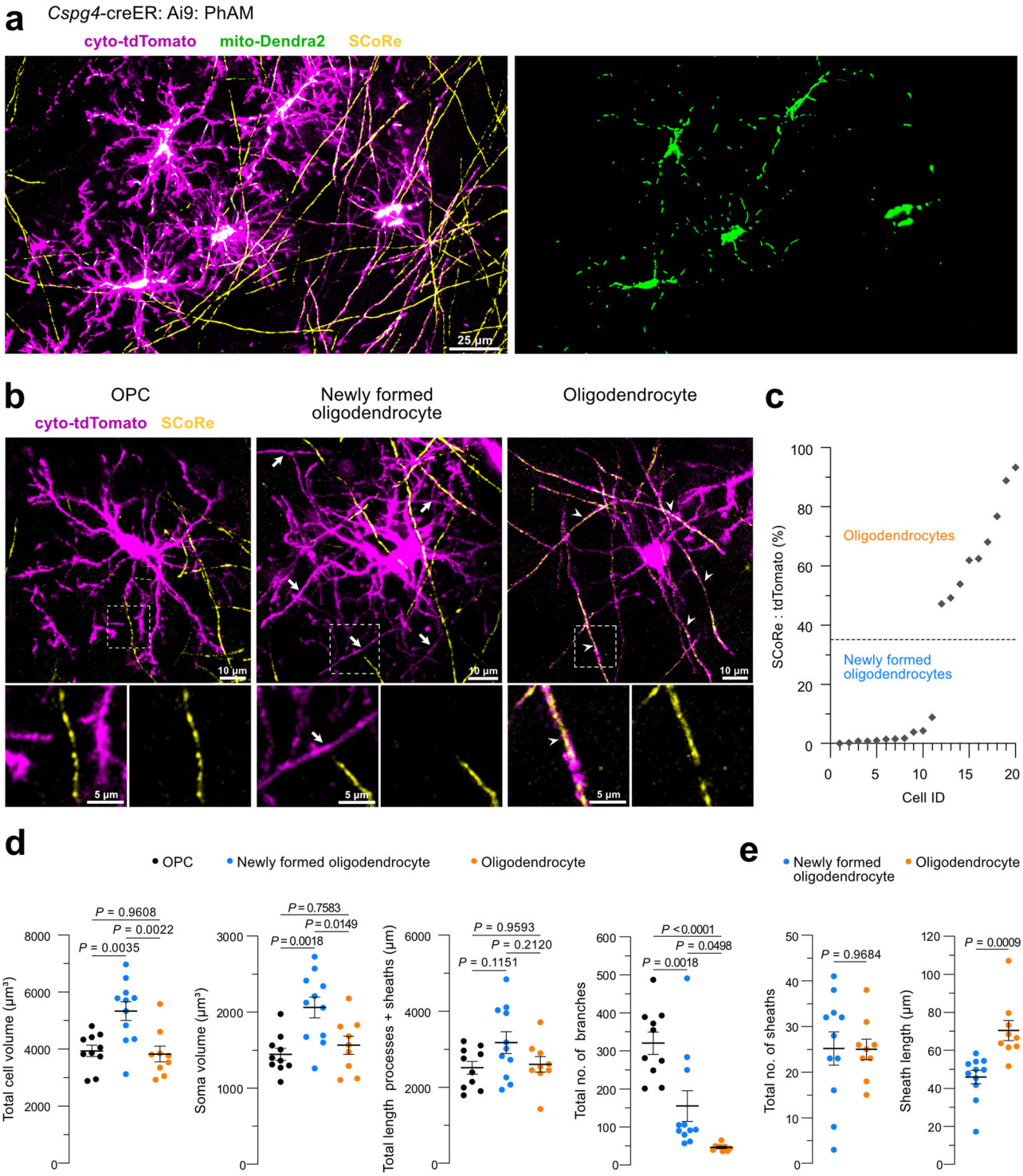

Fig. 1 | In vivo imaging of the oligodendrocyte lineage and their mitochondria. **a** In vivo image captured from the *Cspg4*-creER: Ai9: PhAM mouse cerebral cortex with labeling of mitochondria (green) in the oligodendrocyte lineage (magenta). Spectral confocal reflectance microscopy (SCoRe, yellow) reveals compact myelin sheaths. The images were captured from multiple cranial window positions from 6 mice. **b** In vivo images showing the morphology of an OPC (left), newly formed oligodendrocyte (middle), and mature oligodendrocyte (right). Lack of SCoRe signal in the newly formed oligodendrocyte sheaths (arrows) and presence of SCoRe signal in the sheaths coming from a mature oligodendrocyte (arrowheads). **c** Quantification of SCoRe coverage along the sheaths displayed as a SCoRe to cytoplasmic tdTomato ratio. Cells with high SCoRe coverage in the sheaths (> 34.54%) were grouped as mature oligodendrocytes. Cells with low SCoRe coverage in the sheaths (< 34.54%) were grouped as newly formed oligodendrocytes ($n = 20$ cells from 6 mice). **d** Newly formed oligodendrocytes occupy the highest total cell and soma volume. Total length of processes (+ sheaths when present) is comparable among all three stages, while the total number of branches per cell is highest for the OPCs ($n = 10$ OPCs, 11 newly formed and 9 mature oligodendrocytes from 6 mice, one-way ANOVA, Tukey's multiple comparisons test, the line is at the mean ± s.e.m). **e** Total number of sheaths produced by newly formed and mature oligodendrocytes is similar, while the average length of the sheaths from mature oligodendrocytes is greater ($n = 11$ newly formed and 9 mature oligodendrocytes from 6 mice, unpaired two-tailed t-test, the line is at the mean ± s.e.m). Source data are provided as a Source Data file.

https://doi.org/10.1038/s41467-024-51016-2

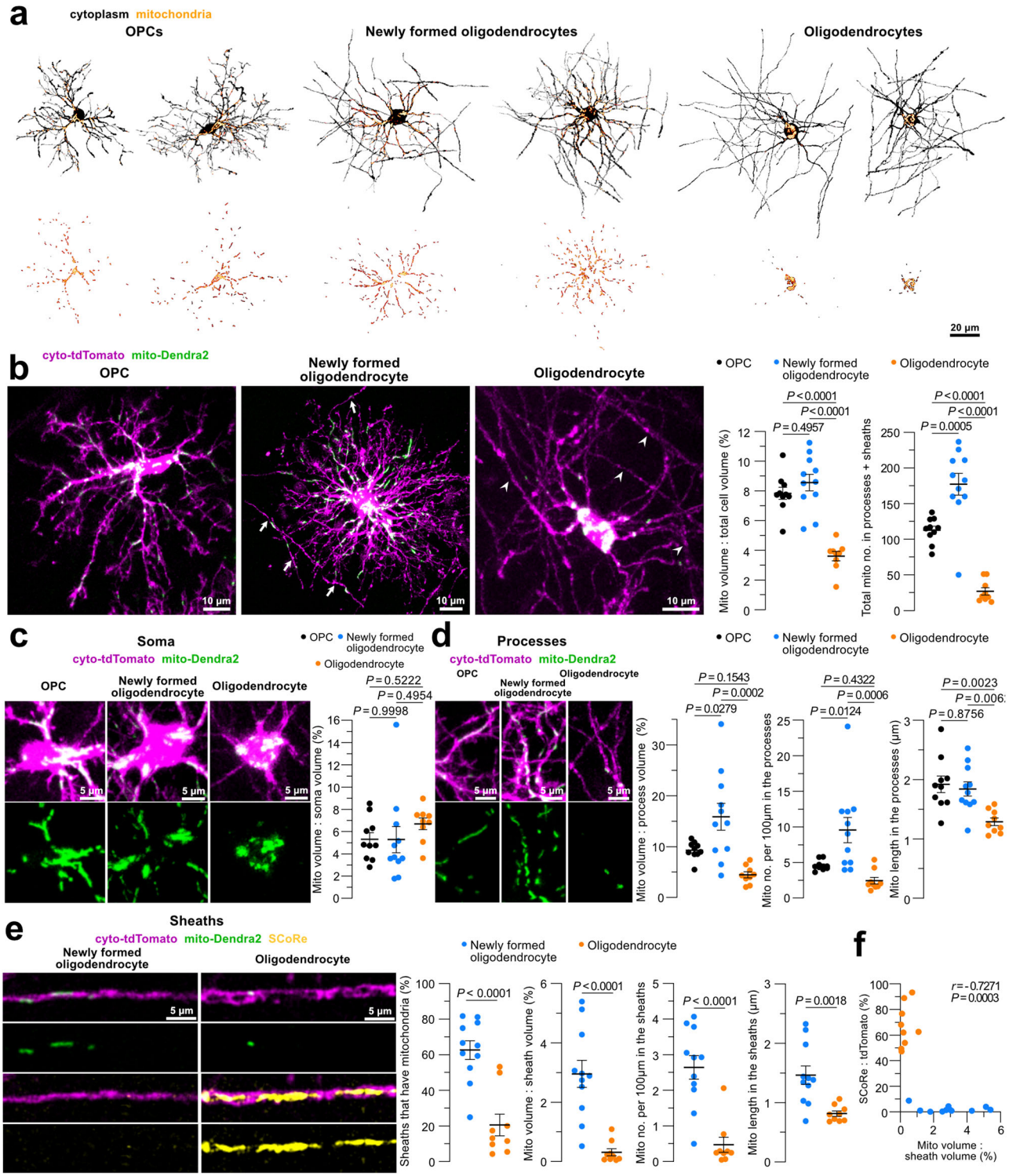

Fig. 2 | Mitochondrial morphometrics and subcellular partitioning across the oligodendrocyte lineage. a 3-D reconstructions of oligodendrocyte lineage cells and their mitochondria. **b** In vivo images of oligodendrocyte lineage cells and their mitochondria. Arrows indicate non-compact sheaths and arrowheads indicate compact sheaths. Total mitochondrial volume fraction per cell, shown as a ratio of total mitochondrial volume to total cytoplasm volume, is lowest in the mature oligodendrocytes. The total number of mitochondria in the processes (+sheaths when present) is highest in the newly formed oligodendrocytes. **c** Mitochondria in the soma of oligodendrocyte lineage cells showing no significant difference among the three stages. **d** Mitochondria in the processes of oligodendrocyte lineage cells showing that volume fraction and density are highest in the processes of newly formed oligodendrocytes, and the average mitochondrial length is the lowest in the processes of mature oligodendrocytes (for **(b), (c), (d)**: $n = 10$ OPCs, 11 newly formed and 9 mature oligodendrocytes from 6 mice, one-way ANOVA, Tukey's multiple comparisons test, the line is at the mean ± s.e.m). **e** Mitochondria in a non-compact newly formed sheath and a compact SCoRe covered sheath from a mature oligodendrocyte. A higher proportion of sheaths from newly formed oligodendrocytes have at least 1 mitochondrion. Sheaths from the newly formed oligodendrocytes have greater mitochondrial volume fraction, density, and length ($n = 11$ newly formed and 9 mature oligodendrocytes from 6 mice, unpaired two-tailed t-test, the line is at the mean ± s.e.m). **f** Negative correlation between mitochondrial distribution in myelin sheaths and myelin compaction determined by SCoRe coverage ($n = 20$ cells from 6 mice, two-tailed Pearson correlation coefficient). Source data are provided as a Source Data file.

https://doi.org/10.1038/s41467-024-51016-2

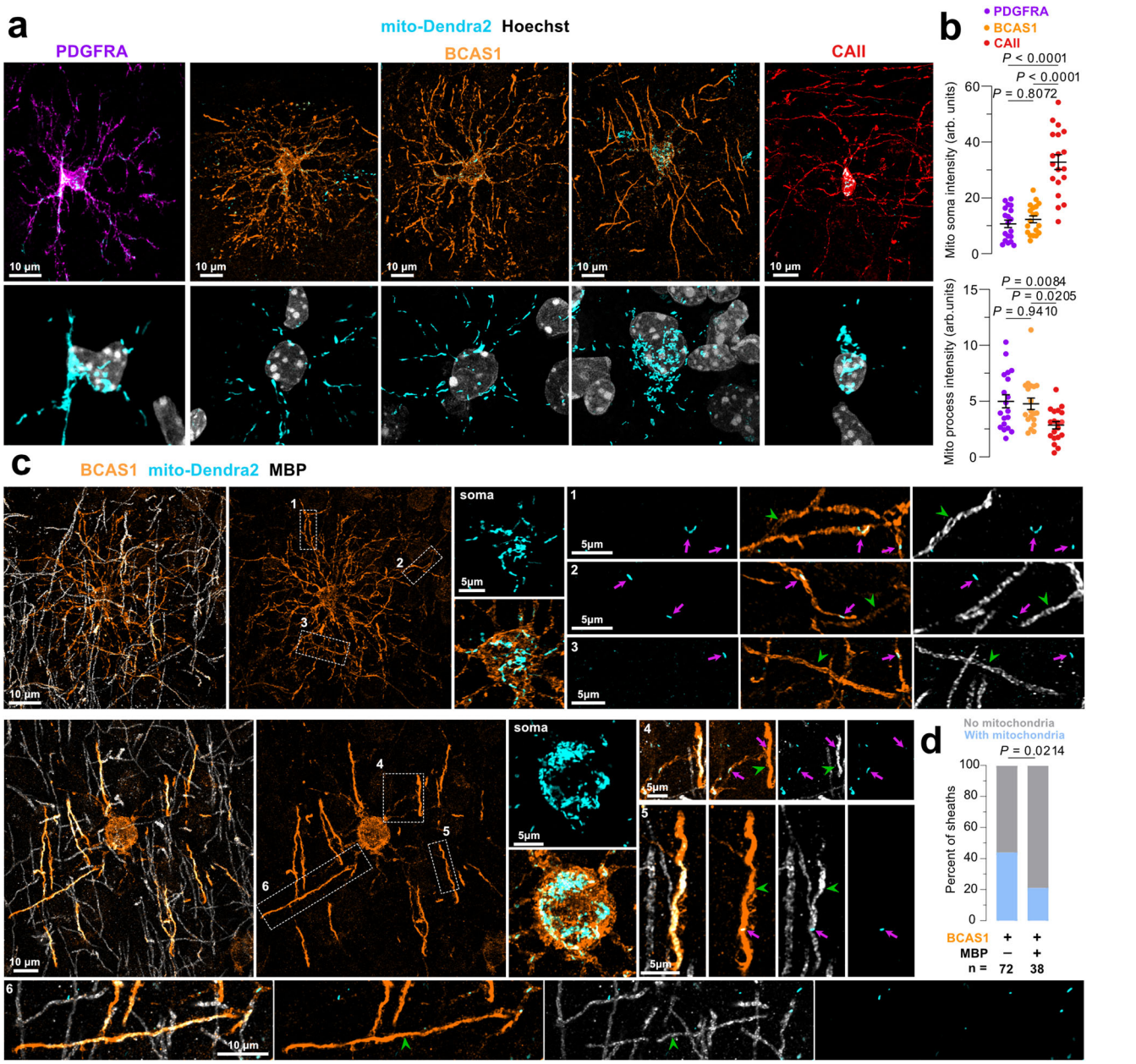

Fig. 3 | Mitochondrial subcellular partitioning across molecularly defined stages of oligodendrocyte maturation. a Representative images of PDGFRA, BCAS1, and CAII labeled cells and their mitochondria. The images in the second row are cropped views of the mitochondria surrounding the cell nuclei from the corresponding cell in the first row. **b** Quantification of mitochondria content within the soma and processes showing that CAII-labeled cells have the highest mitochondrial content in the soma and the lowest in the processes ($n = 19$ cells per each stage from 4 mice, one-way ANOVA, Tukey's multiple comparisons test, the line is at the mean ± s.e.m). **c** Representative images of mitochondria across different compartments of BCAS1-labeled cells: soma, processes, and sheaths. MBP staining represents more mature myelin sheaths. Green arrowheads indicate BCAS1 and MBP dual-labeled sheaths and magenta arrows indicate mitochondria. Boxed and cropped regions are marked with the corresponding numbers. **d** Quantification of the percentage of BCAS1-labeled sheaths with or without the presence of MBP that contained at least 1 mitochondrion ($n = 72$ single-labeled BCAS1 sheaths and 38 dual-labeled BCAS1 and MBP sheaths from 18 cells from 4 mice, two-tailed Fisher's exact test). Source data are provided as a Source Data file.

Mitochondrial distribution differs between human OPCs and oligodendrocytes

Next, we determined if the mitochondrial features that we observed in the mouse cortical oligodendrocyte lineage were also present in human tissue. We used a publicly available electron microscopy dataset (H01)[39] to segment the mitochondria, cytoplasm, and nuclei in a subset of OPCs and oligodendrocytes from the temporal lobe of a human cerebral cortex sample. OPCs were identified based on their distinct process morphology, elongated shape of their soma and nuclei, and less heterochromatin compared to microglia[40] (Fig. 4). Oligodendrocytes were identified based on their processes terminating on myelin sheaths along with their distinct soma and nuclear morphology (Fig. 4). Human oligodendrocyte soma volumes were smaller compared to OPCs and showed a higher mitochondrial volume fraction (Fig. 4b). Distinct variability was observed from one cell process to the next in both cell types with some processes containing multiple mitochondria and others completely devoid (Fig. 4). Even with this variability, overall mitochondrial volume fraction was greater in the OPC processes compared to the oligodendrocyte processes (Fig. 4c).

https://doi.org/10.1038/s41467-024-51016-2

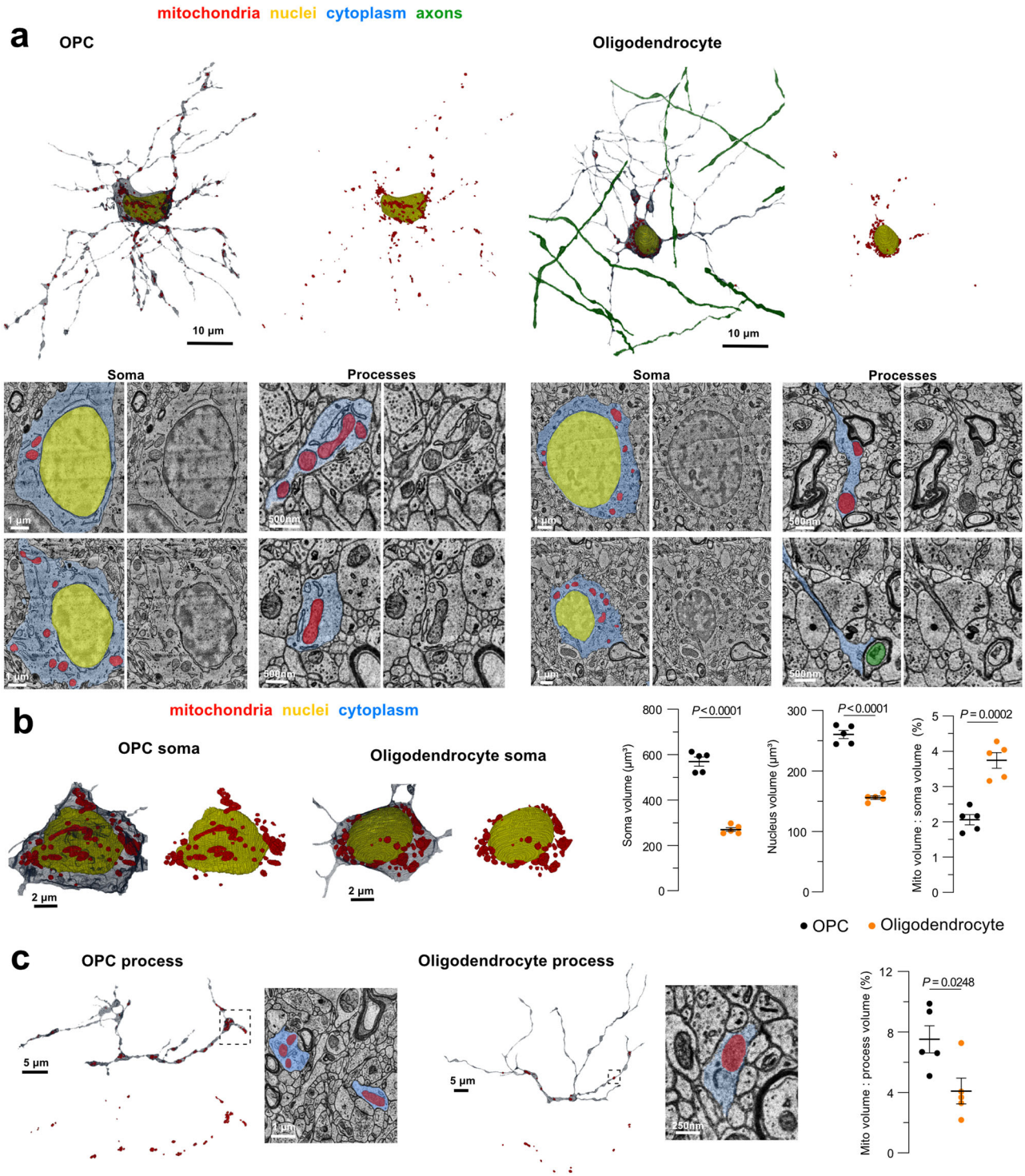

Fig. 4 | Mitochondrial distribution in human OPCs and oligodendrocytes. a 3-D renderings, and example electron micrographs of an OPC and an oligodendrocyte captured from the temporal lobe of a 45-year-old individual showing the mitochondrial distribution and shape in the soma and processes. Several myelinated axons were reconstructed to provide context for the oligodendrocyte processes innervating the myelin sheaths surrounding these axons. The micrographs are representative of 5 OPCs and 5 oligodendrocytes. **b** Example renderings of OPC and oligodendrocyte somas, quantification of soma and nucleus volume, and mitochondrial volume fraction in the soma in the two cell types ($n = 5$ OPCs and 5 oligodendrocytes, unpaired two-tailed t-test, the line is at the mean ± s.e.m). **c** Example renderings of OPC and oligodendrocyte processes and quantification of mitochondrial volume fraction in the processes in the two cell types ($n = 5$ OPCs and 5 oligodendrocytes, unpaired two-tailed t-test, the line is at the mean ± s.e.m). Source data are provided as a Source Data file.

These data confirm the differences in mitochondria localization across the lineage in both the mouse and human, with preferential localization in the soma of the oligodendrocytes and the processes of the OPCs.

Transient mitochondrial network reorganization during oligodendrocyte generation

After determining the mitochondrial localization, content, and shape at single-time-points in different cell stages of the oligodendrocyte

https://doi.org/10.1038/s41467-024-51016-2

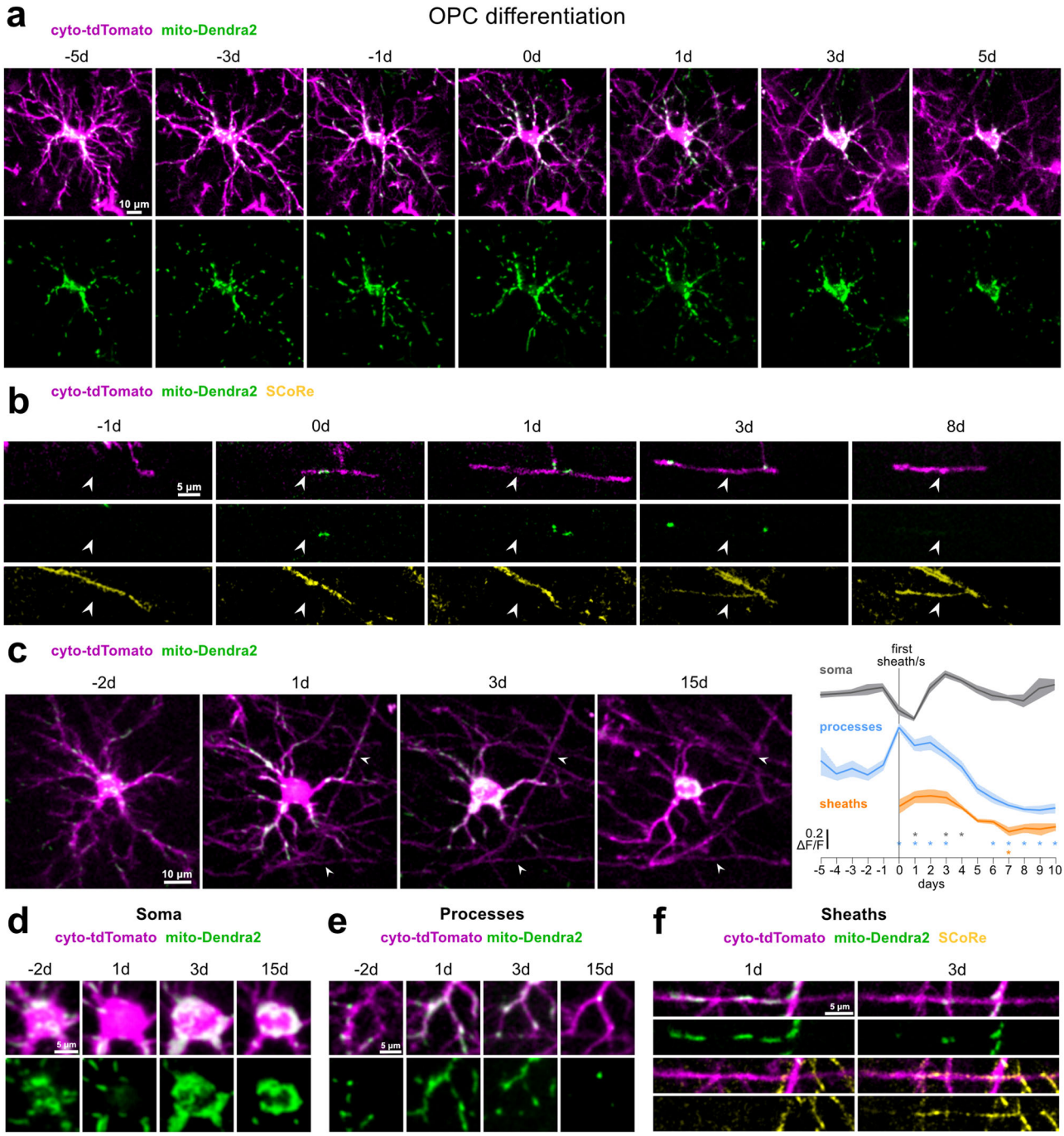

Fig. 5 | Mitochondrial network reorganization and transient expansion during oligodendrocyte generation. a Longitudinal in vivo images of a single differentiating OPC and its mitochondria. Day 0 represents the first day when sheath/s are seen attached to this cell. **b** Image series depicting a myelin sheath (arrowheads), its mitochondria and SCoRe coverage over time. The sheath forms at day 0 and compaction starts 3 days after. **c** Representative images of a differentiating OPC and quantification of changes in mean mitochondrial intensity over 16 consecutive days (5 days before, day of and 10 days after sheath/s formation, $n = 7$ differentiating OPCs from 4 mice, the asterisks indicate data points that significantly deviate from 0 at the 99% confidence interval, the traces represent the mean and the error bands the s.e.m). Mitochondrial intensity decreases in the soma coincident with an increase in the processes as sheaths are formed. Two days later, mitochondrial intensity in the soma increases coincident with a drop of mitochondria in the processes and sheaths. **d**–**f** Changes in mitochondrial distribution over time in the soma **(d)**, processes **(e)**, and sheaths **(f)** of the cell in **(c)**. The images were captured from at least 7 differentiating OPCs over time. Source data are provided as a Source Data file.

lineage, we next performed longitudinal imaging for 20 to 40 consecutive days during P70-P110 to track the mitochondrial changes in the same cell over time. During this period, some of the labeled OPCs spontaneously differentiated into mature, myelinating oligodendrocytes (Fig. 5, Supplementary Fig. 7–9 and Supplementary Movie 1). We denoted the day when the first sheath/s emerged from the newly differentiated cell as day 0 in our analysis. We observed that sheath compaction did not occur until ~3 days later as demonstrated by the appearance of the SCoRe signal in single sheaths (Fig. 5b, f). To determine if there was a stereotyped progression of mitochondrial subcellular localization during differentiation, we quantified changes over time of mitochondrial intensity in each cell compartment (soma,

processes, sheaths) for day 0, as well as 5 days before and 10 days after (Fig. 5c). Mitochondrial intensity in the soma reached the lowest and the highest levels respectively 1 and 3 days after sheath/s emergence (Fig. 5c, d). Additionally, the mitochondrial labeling in the processes peaked on the day of sheath/s formation and decreased over time (Fig. 5c, e). Likewise, mitochondrial content initially peaked in the newly formed sheaths and declined in the days following their emergence (Fig. 5b, c, f). Finally, the circularity of mitochondria in the processes transitioned from the least circular on the day of the first sheath to increasing circularity on the subsequent days of sheath maturation (Supplementary Fig. 9d). Overall, these data show mitochondrial network reorganization and localization away from the cell soma concurrent with migration towards the newly forming sheaths. This transient state is followed by a rapid disappearance of mitochondria in the distal processes and sheaths and the highest mitochondrial content in the soma during oligodendrocyte maturation and myelin compaction.

A potential reason for the transient loss of mitochondria in the soma during differentiation could be the expansion in nucleus size without corresponding expansion in soma size, which could limit the available space for mitochondrial localization in the soma. To test this idea, we performed Hoechst 33342 staining to label the nuclear DNA and measured the nucleus and soma area across the lineage (Supplementary Fig. 5). BCAS1- labeled cells had the largest nucleus and soma size while nucleus-to-soma ratio was the lowest for these cells (Supplementary Fig. 5b). This shows that the cytoplasmic space in the soma excluding the space occupied by the nucleus is still the largest in BCAS1-labeled cells. Therefore, the low mitochondrial content in the soma of early differentiating cells was likely not attributed to the lack of cytoplasmic space.

Mitochondrial subcellular distributions are stable in non-differentiating OPCs and oligodendrocytes

To determine if there were also changes in subcellular mitochondrial localization over time for OPCs that did not change their fate for at least 20 consecutive days, OPCs that spontaneously died, or mature oligodendrocytes, we measured mitochondrial intensity over 10 days in the cell soma, processes, and myelin sheaths (when present) at each stage. For the cells that remained OPCs, no significant differences were seen for the mitochondrial intensity over time in the soma and processes (Supplementary Fig. 8a, Supplementary Fig. 9a, and Supplementary Movie 2). Similarly, mitochondrial intensity in dying OPCs only significantly dropped the day when apoptotic bodies were detected, denoted as day 10, although a rising trend was seen for the mitochondrial content in the processes of the OPCs approaching death (Supplementary Fig. 8b, Supplementary Fig. 9c, and Supplementary Movie 3). Similar to what was observed with changes in mitochondrial circularity during oligodendrocyte differentiation (Supplementary Fig. 9d), mitochondrial circularity decreased in cells that eventually died 2-3 days prior to the fragmentation that immediately preceded cellular death (Supplementary Fig. 9c, e) suggesting an elongated mitochondrial signature during the decision to successfully differentiate or die. Finally, mitochondrial intensity in the soma, processes, and myelin sheaths of mature oligodendrocytes remained stable over time (Supplementary Fig. 8c).

Mitochondrial TFAM labeling differs in somas and processes of the oligodendrocyte lineage cells

The differences we observed in mitochondrial content and subcellar partitioning during oligodendrocyte generation suggested that there are changing mechanisms regulating mitochondrial maintenance during this fate transition. One protein that can regulate mitochondrial maintenance is mitochondrial transcription factor A (TFAM), which is involved in mitochondrial DNA transcription, replication, and its packaging into nucleoids[41]. Therefore, we immunostained and analyzed TFAM labeling and area fraction within a sample of mitochondria networks in the soma and processes of PDGFRA-labeled OPCs, BCAS1-labeled newly formed oligodendrocytes, and CAII-labeled mature oligodendrocytes (Fig. 6). This analysis revealed higher TFAM area fraction values specifically in the mitochondria of BCAS1-labeled cells when compared to the CAII-labeled cells. No difference in TFAM coverage was seen for the PDGFRA- and CAII-labeled groups (Fig. 6). Furthermore, TFAM area fraction values were higher in the soma than in the processes of all oligodendrocyte lineage cells regardless of their stage (Fig. 6d). Mitochondria that lacked TFAM were often small (~ $0.2\mu m^2$ in area) and approximately 37% of all mitochondria in the processes of CAII-labeled oligodendrocytes had less than 10% TFAM area fraction values as compared to 16% of mitochondria within BCAS1-labeled cells and 15% of mitochondria within PDGFRα-labeled cells (Fig. 6e). Overall, this shows decreased mitochondrial TFAM following oligodendrocyte generation, especially in the periphery, and hints at changes in mitochondrial DNA content across different subcellular compartments in the oligodendrocyte lineage.

Mitochondrial motility is greater in OPCs than in oligodendrocytes

Given the robust differences we observed in mitochondrial subcellular partitioning over days and weeks, we next tracked the mitochondrial dynamics in the OPCs and oligodendrocytes over hours to minutes. To first determine general mitochondrial redistribution over hours, we photoconverted the mito-Dendra2 fluorescence in the soma of OPCs and oligodendrocytes and followed these cells over time at 4, 24, and 48 hours (Fig. 7). The intensity of the photoconverted mitochondria dropped quickly at 4 hours for the OPCs but remained stable for the oligodendrocytes. Similarly, the decline was greater for the OPCs than for the oligodendrocytes at 24 and 48 hours (Fig. 7c, d). The higher rate of dilution of the photoconverted mitochondrial signal in the OPCs suggested higher mitochondrial motility in these cells. To further test this hypothesis, we imaged cells once a minute over 30 minutes in awake mice and tracked mitochondrial motility in the OPCs and oligodendrocytes. Throughout this timeframe, we observed a mixture of motile and stationary mitochondria in the OPCs (Fig. 8a, b and Supplementary Movie 4) and only stationary mitochondria in the oligodendrocytes (Fig. 8c, d and Supplementary Movie 5). The average mitochondrial displacement per cell was higher in the OPCs compared to oligodendrocytes (Fig. 8e). On average, ~13% of mitochondria in the OPCs traveled above a displacement threshold set to eliminate measurements of mitochondrial oscillations and any awake imaging movement artifacts (see methods), while no mitochondria in the oligodendrocytes traveled above the same displacement threshold (Fig. 8e).

To understand what external factors could have influenced the range of mitochondrial motility in the OPCs (Fig. 8e), we considered both animal sex and animal locomotion during the image acquisition. Animal sex was not a contributing factor revealing no differences in OPC mitochondrial motility between female and male mice ($n = 22$ OPCs from 7 female and 42 OPCs from 12 male mice, unpaired two-tailed t-test, $p = 0.4956$). On the other hand, animal locomotion itself was loosely correlated to mitochondrial motility in the OPCs. Comparing the average animal locomotion velocity and mitochondrial velocity revealed a weak correlation between the two (Fig. 8f). These data suggested that animal locomotion was partially associated with higher OPC mitochondrial motility.

Arousal state influences OPC mitochondrial motility

With animal locomotion partly correlated with mitochondrial motility in the OPCs, we next determined if animal arousal state impacted mitochondrial motility by treating animals with anesthetics or sedatives during the imaging experiments (Fig. 9a). OPC mitochondrial

https://doi.org/10.1038/s41467-024-51016-2

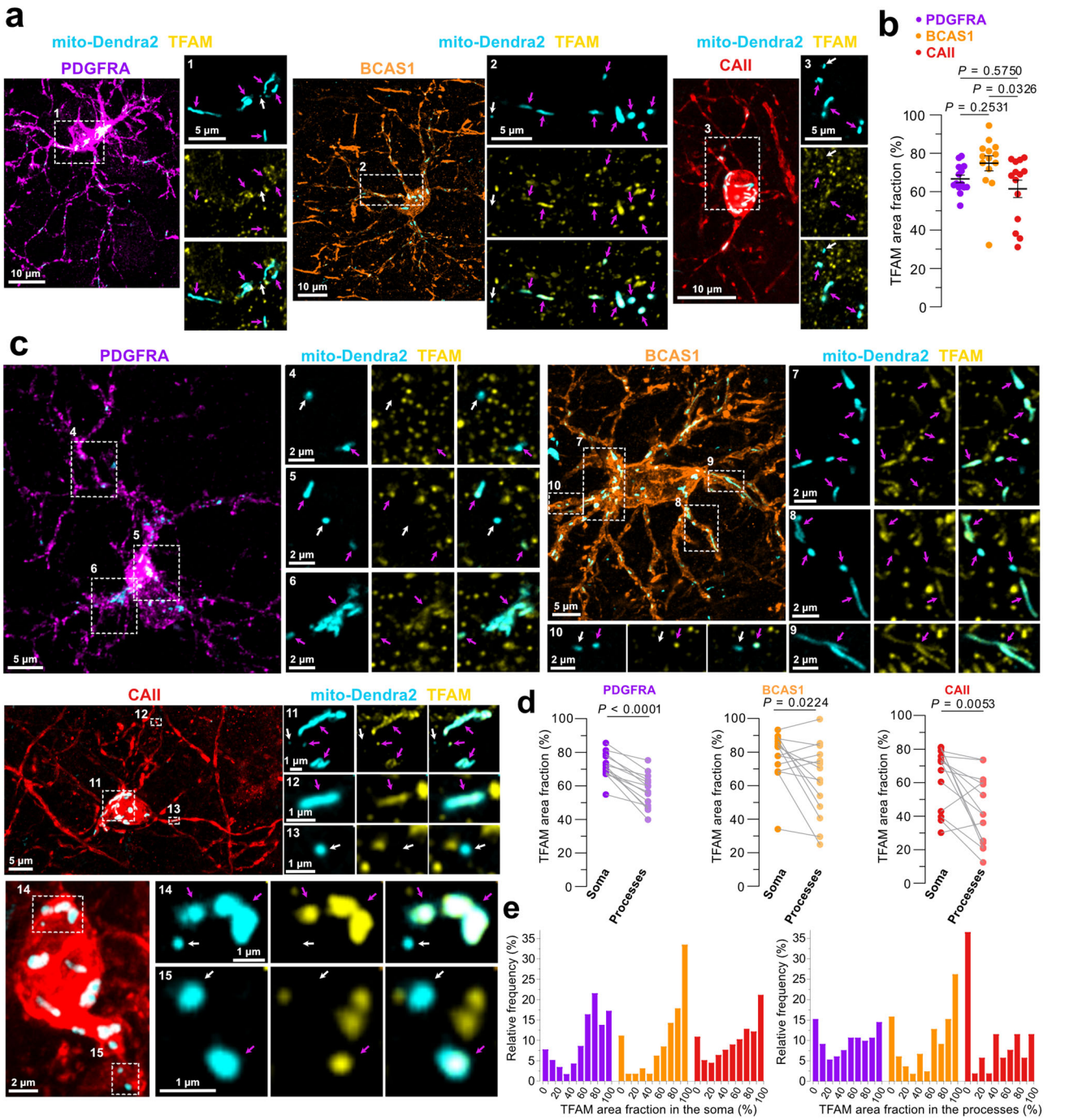

Fig. 6 | TFAM distribution across the different stages and compartments of the oligodendrocyte lineage. a Representative images of TFAM immunofluorescence and mitochondria in PDGFRA, BCAS1, and CAII- labeled cells. Note that TFAM immunostaining labels all TFAM proteins that are present in the tissue, including in the neighboring cells. **b** Quantification of TFAM area fraction in the mitochondria of the oligodendrocyte lineage cells ($n = 14$ cells per each stage from 4 mice, one-way ANOVA, Tukey's multiple comparisons test, the line is at the mean ± s.e.m). **c** Representative images of TFAM labeling in the soma and processes of PDGFRA, BCAS1, and CAII-labeled cells. The boxed images in **a** and **b** represent selected slices from the indicated regions**. d** Quantification of TFAM labeling across cell compartments showed higher TFAM area fraction values in the mitochondria in the soma compared to the processes across all stages ($n = 14$ cells per each stage from 4 mice, paired two-tailed t-test, the line is at the mean ± s.e.m). **e** Frequency distribution of TFAM area fraction values across all mitochondrial networks analyzed in the soma and process at each cell stage ($n = 116$, 224, 156 mitochondrial networks in the soma coming respectively from 14 PDGFRA, BCAS1 and CAII-labeled cells from 4 mice and $n = 131$, 164, 52 mitochondrial networks in the processes coming respectively from 14 PDGFRA, BCAS1 and CAII-labeled cells from 4 mice). Source data are provided as a Source Data file.

motility decreased under both isoflurane (Fig. 9b, Supplementary Fig. 10, and Supplementary Movie 6) and ketamine/xylazine (Fig. 9c, Supplementary Fig. 10, and Supplementary Movie 7) induced anesthesia. Norepinephrine is one of the key neuromodulating signals that change with locomotion and under anesthesia, thus, to test the effects of sedation in addition to anesthesia we next blocked norepinephrine release with dexmedetomidine hydrochloride. Consistent with the other anesthetics, dexmedetomidine treatment decreased OPC mitochondrial motility (Fig. 9d, Supplementary Fig. 10, and Supplementary Movie 8) while no change was observed in vehicle-treated animals

https://doi.org/10.1038/s41467-024-51016-2

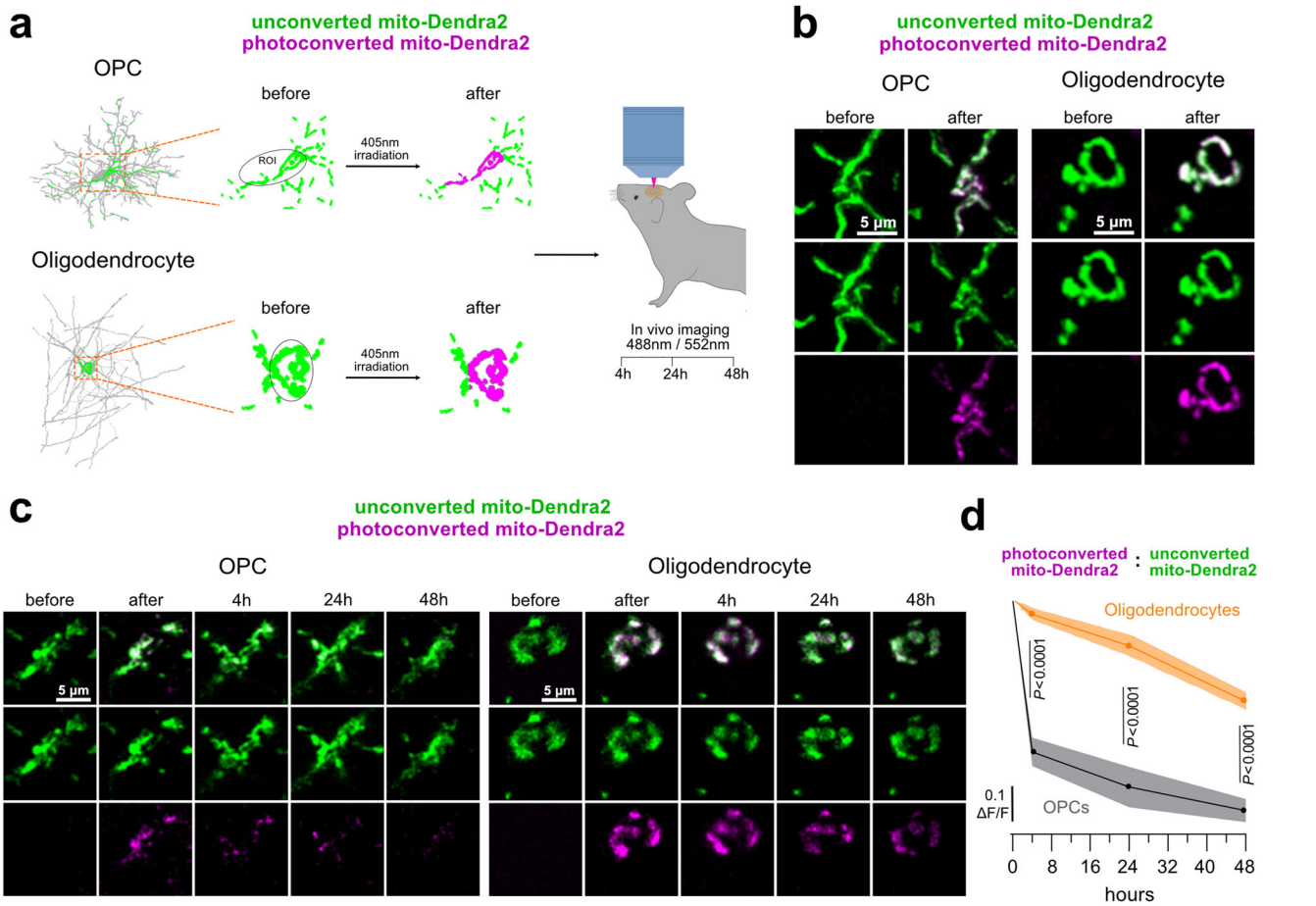

Fig. 7 | Mitochondrial network stability differs between OPCs and oligodendrocytes. a Schematic illustration of photoconversion experiments. A circular ROI was drawn around the soma of mito-Dendra2-only labeled OPCs and mature oligodendrocytes and irradiated with a 405 nm laser. Unconverted and photoconverted mito-Dendra2 signal was imaged in vivo before, immediately after, and at 4, 24, and 48 hours after photoconversion. **b** Example images of mitochondria signal in an OPC and an oligodendrocyte before and after photoconversion. The images are representative of photoconversion from 11 OPCs and 12 oligodendrocytes. **c** Longitudinal images of mitochondria before, after, and at 4, 24, and 48 hours after photoconverting soma mitochondria in an OPC and an oligodendrocyte. **d** Normalized photoconverted to unconverted mitochondria ratios within the soma ROI at 4, 24, and 48 hours after photoconversion showing a rapid loss in photoconverted mitochondria in the OPCs while photoconverted mitochondria in the oligodendrocytes persist for days ($n = 11$ OPCs and 12 oligodendrocytes from 4 mice, multiple unpaired two-sample t-tests with Holm-Šídák method, the traces represent the mean and the error bands the s.e.m). Source data are provided as a Source Data file.

(Fig. 9e, Supplementary Fig. 10, and Supplementary Movie 9). Since oligodendrocyte mitochondria are largely stationary over the 30 min imaging periods, animal anesthesia did not impact the overall motility of mitochondria in mature oligodendrocytes (Supplementary Fig. 10). These results reveal that the animal arousal state influences OPC mitochondrial motility and opens a target for manipulating mitochondrial dynamics in OPCs.

Aged OPCs display reduced mitochondrial length and motility

Given the importance of mitochondria for cellular homeostasis and differentiation, we next characterized the mitochondrial morphology and distribution in aged OPCs which have a reduced capacity to differentiate[35]. We segmented in 3-D a subset of young and aged OPC processes and their mitochondria from high-resolution single-time-point images coming from mice aged either 1 month or 18-21 months (Fig. 10a). Sholl analyses revealed fewer intersections in aged OPCs (Fig. 10b). The mitochondrial volume fraction was decreased in aged OPCs while the density did not change (Fig. 10b). Aged OPCs displayed shorter mitochondrial length, likely accounting for the reduced mitochondria volume in these cells (Fig. 10b). Finally, we imaged mitochondria motility for 30 minutes in awake aged mice. While the percent mitochondria moving in young and aged OPCs did not reach a statistically significant difference between the two groups, aged OPC mitochondria exhibited a lower average displacement suggesting decreased overall mitochondrial motility within the aged OPCs (Fig. 10c and Supplementary Movie 10). Thus, aged OPCs contained shorter mitochondria that moved less.

Discussion

The organelle dynamics that take place before, during, and after fate transitions in the oligodendrocyte lineage are largely unknown. In this study, we generated a transgenic mouse that enables visualization of mitochondria specifically in the oligodendrocyte lineage. Using high-resolution fluorescence optical imaging coupled with intravital longitudinal and label-free approaches, we characterized how mitochondrial content, shape, and motility change in different stages and fates of the oligodendrocyte lineage. During OPC differentiation, mitochondrial content in the processes increased as sheaths were being made and dropped as sheaths formed compact myelin. Mitochondrial shape transitioned from more elongated in OPCs to shorter and punctate in mature oligodendrocytes. In addition, oligodendrocyte mitochondria were stationary while OPC mitochondria were more dynamic. Animal sedation decreased OPC mitochondrial motility and aged OPCs had shorter mitochondria

https://doi.org/10.1038/s41467-024-51016-2

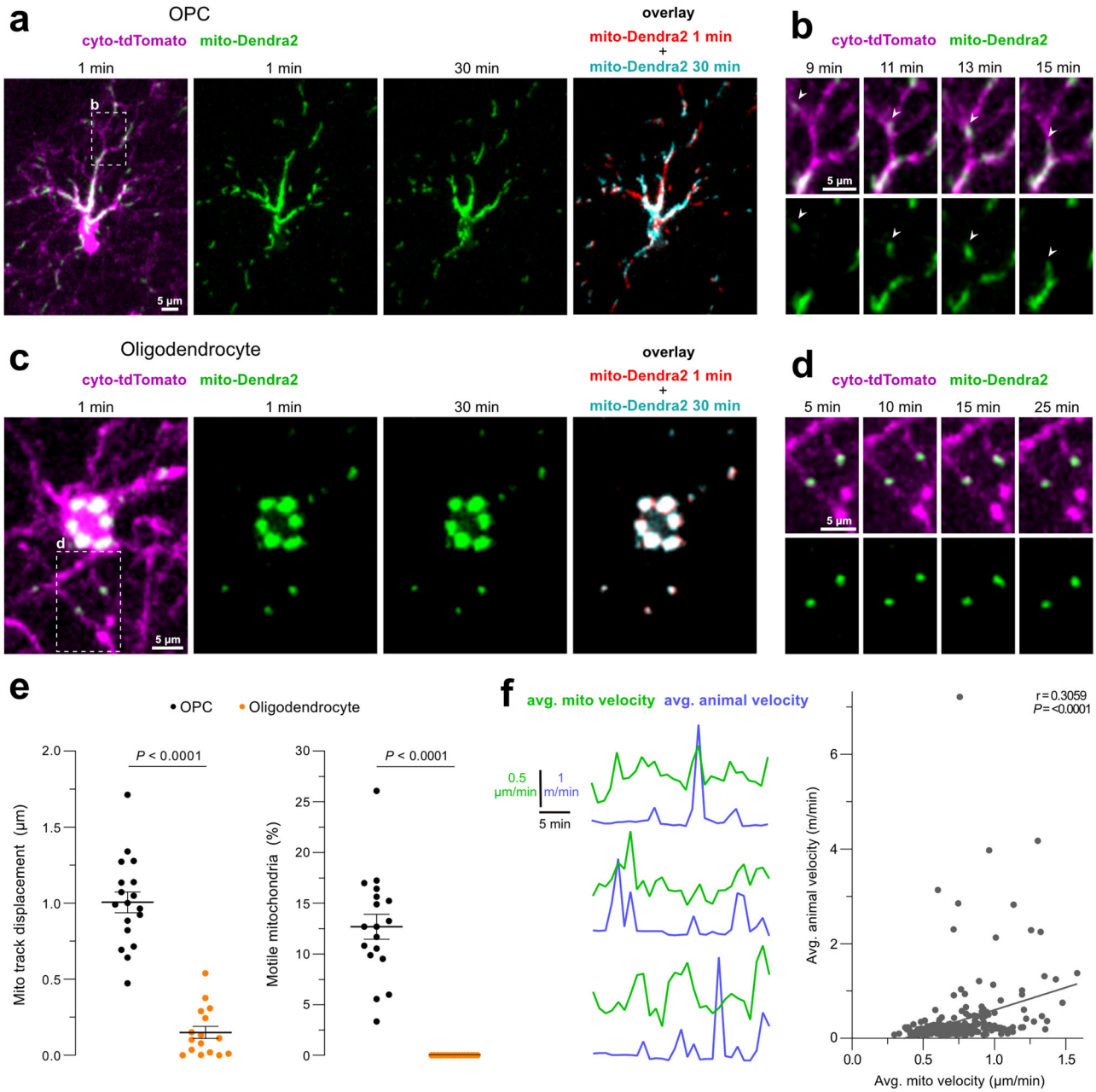

Fig. 8 | Mitochondria are motile in OPCs and stationary in oligodendrocytes. a, c Representative in vivo images of an OPC **(a)** and an oligodendrocyte **(c)** at the first and last minute of a 30-minute time series captured from an awake mouse. The overlay of mitochondria signal at these two time points shows numerous motile mitochondria in the OPC but none in the oligodendrocyte. **b** The boxed region in **(a)** between minutes 9 and 15 of the time series. Arrowheads point at mitochondria moving in the OPC processes. **d** Boxed region in **(c)** showing stationary mitochondria in the oligodendrocyte between minutes 5 and 25 of the time series. The images in a-d are representative of at least 18 OPCs and 16 oligodendrocytes. **e** Mitochondria displacement is greater in the OPCs compared to oligodendrocytes. Percentage of mitochondria per cell that displace 2.4 microns or more over the 30-minute time series, showing that mitochondria in OPCs are motile while oligodendrocyte mitochondria are stationary ($n = 18$ OPCs from 6 mice and 16 oligodendrocytes from 5 mice, unpaired two-tailed t-test, the line is at the mean ± s.e.m). **f** Representative traces of average animal velocity and average velocity of mitochondria within OPCs. Weak correlation between animal locomotion velocity and mitochondria velocity ($n = 261$ events captured from 31 OPCs from 9 animals across the 30-minute time series, two-tailed Pearson correlation coefficient). Source data are provided as a Source Data file.

that moved less. Overall, these data reveal that mitochondria are dynamically positioned within OPCs undergoing fate decisions in the live cerebral cortex. This provides insight into identifying important temporal windows for when these changes occur and how subcellular organelle dynamics could impact oligodendrocyte generation. In addition, it provides a way to more precisely determine the maturity stages in the oligodendrocyte lineage based on mitochondrial shape, content, and location that cannot be distinguished from the existing molecular markers alone.

Mitochondrial distribution, shape, and motility are closely linked to mitochondrial function[16,34,42–44]. The increase in mitochondrial content during OPC differentiation can be attributed to the role for mitochondria in providing energy and substrates for lipid synthesis[45]. Indeed, high levels of ATP are needed for the formation of myelin sheaths[46,47] and impairing mitochondria has been shown to reduce myelin lipids in the peripheral nervous system[48]. Given the long life of myelin components[1,49], the energy requirements for maintaining the myelin sheaths are likely lower than for synthesizing them which could

https://doi.org/10.1038/s41467-024-51016-2

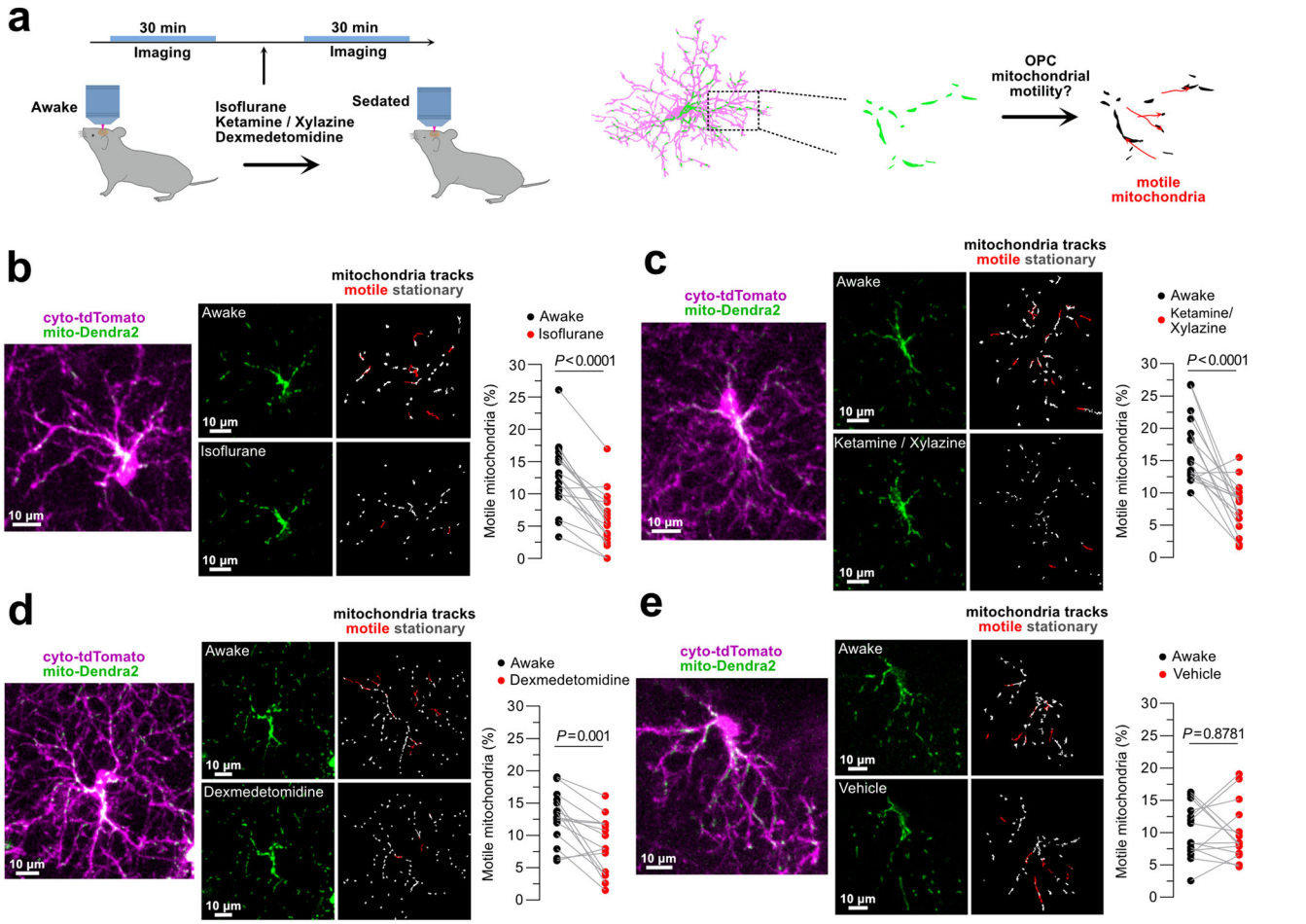

Fig. 9 | Animal sedation decreases mitochondrial motility in OPCs. a Schematic illustration of experimental timeline. Animals were imaged for 30 minutes in awake and anesthetized/sedated conditions and mitochondria in the OPCs were analyzed to determine their motility rate. **b**–**e** Left of each panel: representative images of mitochondrial subcellular distribution in the analyzed OPCs at the start of the awake imaging session. Right of each panel: mitochondrial signal at the start of each imaging session in each condition along with mitochondrial tracks only in the processes of the targeted OPCs across 30 minutes for the awake and 0.8–1% isoflurane (**b,** $n = 18$ OPCs from 6 mice, paired two-tailed t-test), 100 mgkg^{-1} ketamine/10 mgkg^{-1} xylazine (**c,** $n = 17$ OPCs from 5 mice, paired two-tailed t-test), 0.5 mgkg^{-1} dexmedetomidine hydrochloride (**d,** $n = 15$ OPCs from 4 mice, paired two-tailed t-test) and vehicle conditions (**e,** $n = 14$ OPCs from 4 mice, paired two-tailed t-test). Tracks in red represent mitochondrial displacement of 2.4 µm or greater and are referred to as "motile". All the conditions in **(b), (c)**, and **(d)** reduced mitochondrial motility compared to awake conditions. Source data are provided as a Source Data file.

explain the drop in mitochondrial content as sheaths mature. As myelin sheaths compact, they exclude the cytoplasmic content and hence reduce the available space for the organelles which is consistent with the decline in mitochondrial content with compaction. Additionally, similar to mitochondria, peroxisomes have also been described in regions of non-compact myelin[50].

At our single-time-point analysis using both morphological and immunohistochemical criteria, we were not able to distinguish exactly when changes in mitochondrial content took place as we labeled and analyzed a continuum of cell states in the oligodendrocyte lineage, thus explaining some of the data variability, particularly in the newly formed oligodendrocytes group (Fig. 2). Longitudinal imaging clarified when and how mitochondrial partitioning occurred and confirmed that even within days mitochondrial content can change drastically during oligodendrocyte generation (Fig. 5). For example, we saw that mitochondria in the soma of the newly formed oligodendrocytes reached both the lowest and highest mitochondrial content within 3 days. A potential reason for mitochondria leaving the soma is to assist in the tips of the processes as the sheaths are formed and initiate compaction. In support of this, an earlier study suggested that mitochondria in the processes are more active at this stage than the mitochondria in the soma[51]. Once the sheaths are formed and compact, mitochondria either return to the soma and/or get locally degraded which due to technical limitations, we have not been able to distinguish. Mitochondrial degradation could explain the decline in mitochondrial content during oligodendrocyte differentiation which occurs over several days until it reaches a low steady state density. Consistent with this, previous work suggests that mitophagy is a prerequisite for oligodendrocyte generation[28]. Moreover, mitochondrial fragmentation has been shown to precede and facilitate mitophagy[52], thus the maturation-dependent decline in mitochondrial length is also consistent with mitophagy.

In addition to changes in mitochondrial shape and localization, we also found changes in TFAM compartmentalization across the lineage with higher TFAM content in BCAS1-labeled differentiating and newly formed oligodendrocytes compared to CAII-labeled mature oligodendrocytes. This could suggest a higher mitochondrial DNA content for these cells, as previously shown for recently differentiated cells in vitro[25], and a potentially higher rate of mitogenesis. However, more experiments are needed to directly measure and validate the rate of mitogenesis in this lineage in vivo. Mitochondria completely lacking or with low TFAM labeling were more common in the processes than the soma of cells at all stages which suggests a different population of mitochondria across these compartments. Indeed, a recent study

https://doi.org/10.1038/s41467-024-51016-2

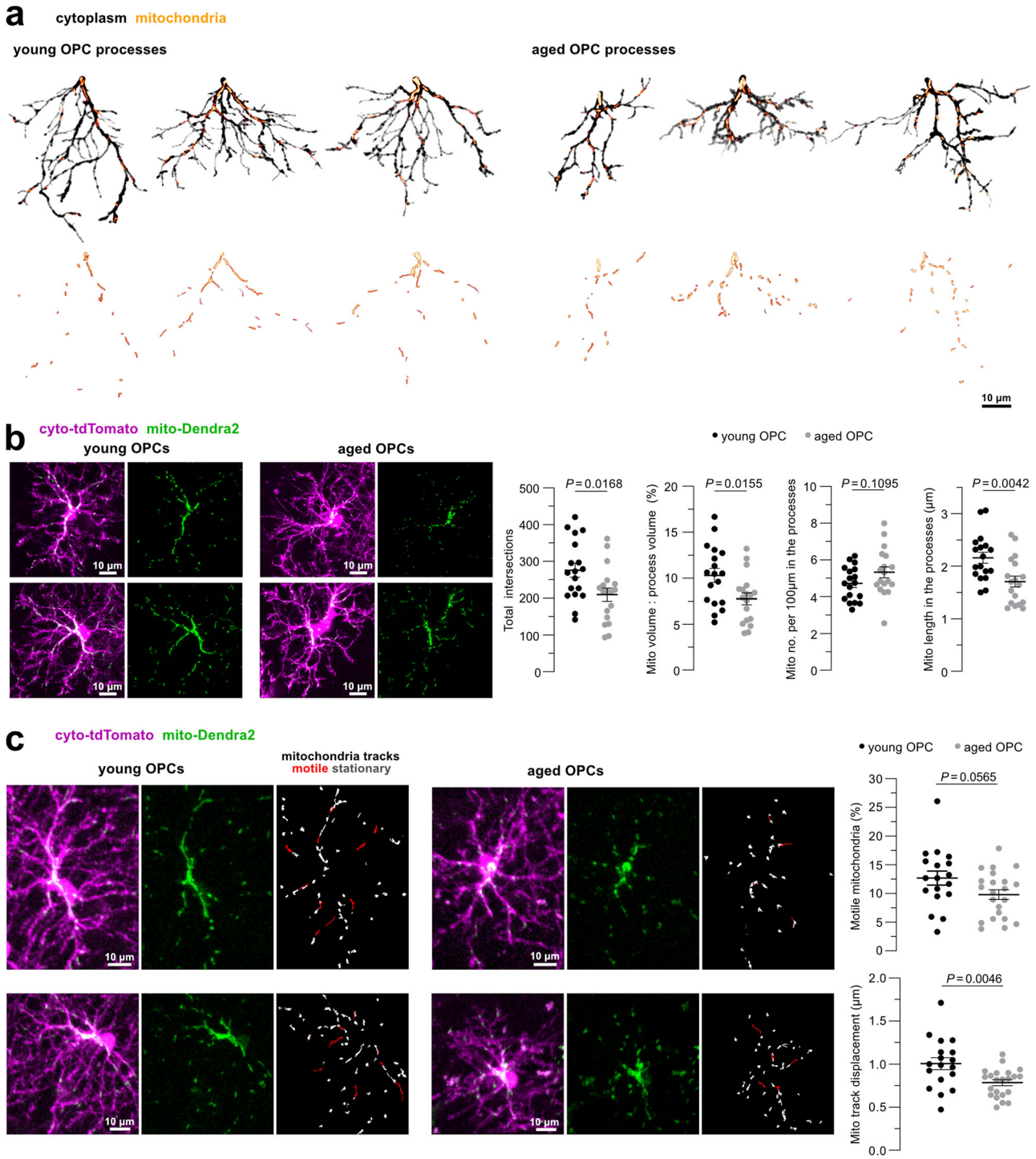

Fig. 10 | Aged OPCs have shorter mitochondria that are less motile. a 3-D reconstructions of a subset of processes and their mitochondria in young and aged OPCs. **b** In vivo images of young and aged OPCs and their mitochondria. Aged OPCs display a lower number of total intersections as quantified by Sholl analysis. Mitochondrial volume fraction is also lower in the processes of aged OPCs while mitochondrial density shown as number of mitochondria per 100 µm is not statistically different. Mitochondria in the processes of aged OPCs are shorter ($n = 18$ OPCs from 4 young mice and 18 OPCs from 6 aged mice, unpaired two-tailed t-test, the line is at the mean ± s.e.m). For **(a)** and **(b)**, young and aged OPCs refer to OPCs coming respectively from mice aged 1 month and 18-21 months. **c** Representative images of mitochondrial subcellular distribution in OPCs at the start of the awake imaging session along with mitochondrial tracks in the analyzed OPC processes that show mitochondrial displacement along the 30-minute imaging series. Tracks in red represent mitochondrial displacement of 2.4 µm or greater and are referred to as "motile". The percentage of mitochondria that move at or above a 2.4 µm threshold and the average displacement of mitochondria in the processes of the aged OPCs ($n = 18$ OPCs from 6 young mice and 22 OPCs from 3 aged mice, unpaired two-tailed t-test, the line is at the mean ± s.e.m). Young and aged OPCs refer to OPCs coming respectively from mice aged 2 months and 18-21 months. Source data are provided as a Source Data file.

found that neuronal mitochondria lacking TFAM are smaller and exhibit different functions than the ones that do not[53]. We also observed that mitochondria lacking TFAM across the lineage often corresponded to a smaller size and given the small size of mitochondria in the processes of oligodendrocytes, this could partially explain why a higher proportion of them (~ 21%) completely lacked TFAM. It is important to acknowledge the limitation in spatial resolution of our optical imaging of TFAM immunofluorescence in this study. Future experiments with increased resolution and alternative ways of assessing mitochondrial DNA content and function are needed to advance these conclusions.

The ultrastructural analyses in the human tissue revealed differences between OPCs and oligodendrocytes with regards to soma and nucleus volume, and mitochondrial subcellular partitioning (Fig. 4). Although some of these differences were more evident than from the single-time-point mouse data which initially showed trends towards differences between these cell populations but not reaching significance (Figs. 1, 2), it is important to note that live measurements from the mouse were taken from cells 20 days after Cre recombination (tamoxifen at P25 and imaging at P45) meaning the mature oligodendrocytes labeled and analyzed were not more than ~15 days "old", with many likely to have differentiated less than 10 days prior to the analyses. While these cells had canonical myelinating oligodendrocyte morphology and were making compact myelin, they were still relatively young, particularly when comparing the age of the cells in the 45-year-old human tissue. Subsequent longitudinal analysis in the mouse revealed changes in soma size during in vivo OPC differentiation with an initial peak immediately following the formation of the first sheath/s followed by a progressive drop as the cell matured (Supplementary Fig. 7). These data are consistent with other reports noting transient increases in oligodendrocyte soma size during differentiation followed by prolonged soma shrinkage with maturation and age[38,54,55]. Moreover, additional measurements of soma size and mitochondrial content in OPCs and oligodendrocytes at P60 (35 days post Cre recombination) revealed significant differences between the two cell types, consistent with the human data (Supplementary Fig. 7). It is also important to note that tissue fixation can significantly alter cell and mitochondrial morphology[56,57], thus it is difficult to make direct comparisons of mitochondrial morphometrics between live cell images and those obtained optically in PFA perfused tissues, or at the ultrastructural level from immersion fixed human tissue. This is particularly evident in the fixed tissue samples that often did not contain as many elongated mitochondria in the OPCs and newly formed oligodendrocytes compared to the mitochondria that were imaged in cells at similar maturation stages in vivo. Despite these variables, our observations reveal a stereotyped and progressive cell morphology change and redistribution of mitochondria within the differentiating cell over weeks. There are abrupt (within hours and days) changes occurring throughout the differentiation event and initial myelin sheath formation, but mitochondrial partitioning continues to gradually change for weeks after oligodendrocyte generation.

Changes in mitochondrial content and shape during oligodendrocyte differentiation are likely interdependent with metabolic transitioning that occurs between high rates of oxidative phosphorylation in OPCs[58,59], increased oxidative metabolism and higher ATP levels in newly formed oligodendrocytes[35], and a switch to glycolysis in oligodendrocytes[60,61]. Likewise, longer mitochondria are generally associated with increased rates of oxidative phosphorylation[62,63] although this varies depending on the cell type and cellular context[34,64]. In addition to providing metabolic substrates, mitochondria could also be buffering calcium in defined subcellular compartments. Mitochondria localized in the processes of the OPCs and immature oligodendrocytes are thought to be important for maintaining calcium homeostasis[51,65]. In addition, mitochondria have been linked to calcium transients in newly forming myelin sheaths which decline with myelin maturation[66]. Lastly, mitochondria are a central player of cellular death. High mitochondrial content during oligodendrocyte differentiation could be linked to the increased susceptibility towards oxidative stress and mitochondria disruption at this stage[25,35,67]. Our longitudinal imaging showed a trend toward increased mitochondrial content in the processes of the OPCs before the formation of apoptotic bodies and death. While not statistically significant based on our cutoff (Supplementary Fig. 8b), it is likely that this trend signifies the initiation of an oligodendrocyte differentiation program but a failure to survive and integrate due to unfavorable intra- and extracellular signals. This idea is also supported by the decrease in mitochondrial circularity days before OPC death similar to what was observed during the early stages of sheath formation in differentiating cells (Supplementary Fig. 9d, e).

Mitochondria move within the cell to relocate to the sites where they are needed[42–44]. Our data show that mitochondrial motility and overall dynamics were higher in OPCs compared to mature oligodendrocytes (Figs. 7, 8). Consistent with this, mitochondrial motility in neurons decreases with their maturation[68,69] and corresponds to increased levels of syntaphilin[70], a mitochondrial docking protein whose levels also change with oligodendrocyte maturation[71]. Moreover, mitochondrial motility in neurons and astrocytes in vivo is lower compared to in vitro or ex vivo slice studies[68,72–74]. Similarly, we saw that oligodendrocyte mitochondria were more stationary in vivo than what had been reported in slices[31] and cultured oligodendrocytes[32]. Other than the physiological context, the maturation state of these cells could also contribute to this discrepancy as the age of the oligodendrocyte, even if expressing many mature oligodendrocyte markers (as discussed above), is likely different between these studies. Additionally, the in vivo system better models the neuronal activity and neurotransmitter release that happens in the native environment of these cells. Our results suggest that the arousal state plays a role in modulating mitochondrial motility in OPCs (Fig. 9). Arousal state has been linked to changes in calcium transients in OPCs and other glia[74–78]. Thus, arousal-dependent changes in mitochondrial motility are consistent with recent evidence of decreased calcium dynamics in OPCs in anesthesia conditions or when norepinephrine release is blocked[75]. Norepinephrine can influence the differentiation and/or proliferation of oligodendrocytes and the expression of norepinephrine receptors in the OPCs changes with their differentiation[75,76,79]. Overall, these observations suggest a potential connection between mitochondria and calcium dynamics and raise questions about how the animal arousal state influences mitochondria in these cells and therefore the cell fate in the oligodendrocyte lineage.

Consistent with reduced mitochondrial trafficking with aging in other cells[80], including neurons[81], aged OPC mitochondria also displayed reduced displacement. In addition, the reduced mitochondrial volume fraction and size could explain the decline in ATP levels and cellular respiration observed in cultured OPCs from aged animals[35]. Aging is associated with increased oxidative stress and decreased mitophagy which could lead to mitochondrial fragmentation and accumulation of damaged mitochondria[33]. This can partially explain why there was a decrease in size of the individual mitochondrial networks and no changes in the mitochondrial density in the aged OPCs. It is also important to note that the mitochondrial morphometrics and motility were variable in the aged OPCs, likely reflecting the documented heterogeneity of OPC states in the aged brain[82]. Whether these are linked to functional heterogeneity between these cells is yet to be determined. Nonetheless, these data point to overall metabolic changes occurring in aged OPCs that would likely impact their ability to successfully generate new oligodendrocytes.

Methods

Animals

The following mouse lines: *Cspg4*-creER[6] (JAX #008538); Ai9[83] (JAX #007909); PhAM[84] (JAX #018385) were bred to generate the *Cspg4*-creER: Ai9: PhAM triple transgenic mice. This mouse line allows for conditional visualization of mitochondria (mito-Dendra2 labeled) and cytoplasm (tdTomato labeled) in cells expressing the chondroitin sulfate proteoglycan 4 (*Cspg4*, also known as NG2) and their progeny. A single dose of tamoxifen (0.4-0.8 mg) was intraperitoneally injected at P25. This produced sparse dual or single recombination providing double and single tdTomato-only or mito-Dendra2-only labeled cells. Both male and female mice aged P30-P651 were used for the experiments. Aged animals (P539-P651) had been used as breeders. All animals were housed in a temperature and humidity-controlled vivarium in a 12 h light/dark cycle with ad libitum access to food and water. All the animal procedures were approved by the Institutional Animal Care and Use Committee at Dartmouth College (protocol number: 00002158).

Surgical procedures

In vivo imaging was performed in acute and chronic cranial windows implanted over the somatosensory cortex. First, the animals were anesthetized via intraperitoneal injections of ketamine/xylazine (100 $mgkg^{-1}$/ 10 $mgkg^{-1}$) or placed under 1% isoflurane. After sterilizing and removing the skin covering the skull, a craniotomy was performed over a 3 by 3 mm area of the exposed skull. The skull and the underlying dura were removed and a circular #0 glass coverslip was positioned on top of the craniotomy region to create an optically accessible imaging window[85]. Carprofen analgesic (5 $mgkg^{-1}$) was administered subcutaneously before and after the surgery as well as in the following 24 and 48 hours. Acute imaging was performed on the day of the surgery after the animals recovered from anesthesia. Chronic imaging was performed after allowing at least 3 weeks for the animals to acclimatize to the surgery.

Imaging

For all anesthetized in vivo imaging experiments, the animals were placed under 0.8-1% isoflurane anesthesia (2% used for induction) and imaged on an upright laser-scanning confocal (Leica SP8) or upright laser-scanning two-photon microscope (Bruker Ultima) with a 20X water immersive objective (respectively Leica NA 1.0 and Zeiss NA 1.0). The tdTomato was excited by 552 nm laser wavelength on the confocal and 1040 nm on the two-photon. Unconverted mito-Dendra2 was excited by 488 nm and 920 nm laser wavelengths from the respective microscopes. SCoRe images were captured on the confocal microscope by overlaying the reflectance from 448 nm, 488 nm, 552 nm, and 637 nm lasers[36,38]. The Z-stacks were taken over a depth of 50-100 μm in layer I of the somatosensory cortex with a 1.5 μm step size. The same settings were used for the awake imaging in which the animal's head was fixed in the Neurotar's Mobile HomeCage setup and the animal could move ad libitum on an air table.

3-dimensional (3-D) reconstructions and single-time-point analysis

3-D reconstructions were used to quantify the mitochondrial density and volume fraction (total mitochondrial volume divided by the total cytoplasmic volume) for each cell and their compartments (soma, primary, secondary, tertiary+ processes, and myelin sheaths) along with mitochondria, processes, and myelin sheaths lengths. We traced a group of cells from single-time-point, high-resolution images, captured from P45-P46 animals following acute cranial window and later separated them into 3 categories: OPCs (polydendritic morphology lacking myelin sheaths), newly formed oligodendrocytes (presence of premature sheaths with less than 34.54% SCoRe coverage), mature oligodendrocytes (presence of compact myelin sheaths with more than 34.54% SCoRe coverage). For the identification of premature myelin sheaths that completely lacked SCoRe signal, the following criteria were used: be a terminal process (no branching), be at least 5 μm in length, and have a larger diameter than the proximal process.

The cells of interest were cropped, smoothed, and traced in 3-D using the Simple Neurite Tracer (SNT, version 4.1.2) Fiji Plugin[86,87]. Tracing was done based on the cytoplasmic localized tdTomato signal for all the cell compartments for which we could unambiguously determine that they were attached to the cell. The soma was marked by a single-point path placed in the center. A segment path was created along the length of the processes and myelin sheaths. A separate path was created at every branching point and the order of branching was noted. The initial processes emerging from the soma were considered primary, their immediate branches were considered secondary, and the branches coming from secondary processes and above were denoted as tertiary+. Only the myelin sheaths for which we could assign a myelinating process were traced. Similarly, mitochondria were traced along their length throughout every cell compartment and noted accordingly to which compartment they belonged. All the traced paths were then filled using the "Fill out" command from the SNT Path Manager menu. A threshold was set so that all the corresponding signals along the path were accurately included in the fill. Different thresholds were set to match the thickness of the traced structure. The volume values for the cytoplasmic and mitochondrial channels were exported from the fills. Additionally, the path lengths were measured using the "Measure path" command from the SNT Path Manager menu. The "Analyze Particles" command was run on the SNT-reconstructed mitochondria to determine their corresponding ROIs and their circularity and aspect ratio were automatically calculated from the shape descriptors in Fiji. Similarly, SNT reconstructions were generated to analyze the images captured from young and aged animals (respectively P30-P35 and P539-P651). In this case, a subset of processes was selected per cell, including a primary process emerging from the soma and all the subsequent branches. The experimenter was blinded to the age of the animal and the mitochondrial channel when selecting the processes to be analyzed. Sholl analysis was performed in Z-projections of reconstructed images using the SNT "Sholl Analysis" command[88] to determine the total number of intersections. The tip of the primary process was set as the center, the start radius was set at 0 μm, the step size was set at 1 μm and the end radius at 70 μm.

The single-time-point soma area analysis was done for cells at P60 (5 weeks post tamoxifen administration). Z-projections were created from the cropped stacks of cells of interest and smoothed. A circular region of interest (ROI) was drawn around the cell soma using only the cytoplasmic channel as a reference. The area and mean intensity of the mitochondrial signal within the ROI were measured in Fiji. The latter corresponded to the ratio between the sum of the intensity of the pixel values included in the ROI and the total number of pixels in the defined region.

SCoRe analysis

SCoRe coverage was analyzed to determine the level of compaction in the newly formed and mature myelin sheaths coming from newly formed or mature oligodendrocytes. The SCoRe channels were merged into a single channel which was later smoothed and thresholded by running the Robust Automatic Threshold Selection in Fiji. The same threshold method was applied to the cytoplasmic channel. Only a sample of the sheaths that had no overlapping signal (from either background or other sheaths and structures in the territory) were traced using SNT and filled out for both the SCoRe and the cytoplasmic channels to generate ROIs of the sheath of interest. The integrated density within the given ROIs was measured and ratios of the SCoRe to cytoplasmic signal in the sheaths were analyzed. K-means clustering was run to determine the threshold for high versus low SCoRe coverage in our dataset (k = 2, threshold = 34.54%).

Immunohistochemistry and analysis

At the end of the in vivo imaging, falling at P130, the animals were anesthetized and transcardially perfused with 4% paraformaldehyde solution diluted in 1X PBS. Following dissection, the brains were fixed for 24 hours in the same solution at 4 °C before switching to 1X PBS only. Next, 75 µm thick free-floating slices of the forebrain were cut on a vibratome and cryopreserved at −20 °C. To perform antigen retrieval, tissue sections were incubated for 2 minutes at 95 °C in a pre-heated buffer solution containing 10 mM Tris, 1 mM EDTA, and 0.05% Tween 20 at pH 9. Tissue sections were incubated in primary and secondary antibodies diluted in 0.3% Triton X-100 and 1% Bovine Serum Albumin in 1X PBS, respectively, for 24 and 2 hours at room temperature. The sections were washed three times in 1X PBS before and after the incubations. When needed, DNA staining was performed at the end of the immunostaining by incubating the tissue sections in a 10 mg/ml Hoechst 33342 solution (Thermo Fisher Scientific, Catalog #: H3570) diluted at 1:2000 in 0.3% Triton X-100 in 1X PBS for 30 minutes. The sections were mounted with ProLong Diamond mountant and imaged with the confocal microscope with a 63X oil immersive objective (Leica NA 1.4). Two to three brain sections were imaged per animal. Primary antibodies used include: goat anti-PDGFRα (1:1000, R&D Systems, Catalog #: AF1062), guinea pig anti-BCAS1 (1:750, Synaptic Systems, Catalog #: 445 004), mouse anti-CAII (1:500, Santa Cruz Biotechnology, Catalog #: sc-48351), rabbit anti-MBP (1:1000, Abcam, Catalog #: ab40390), rabbit anti-TOM20 (1:200, Abcam, Catalog #: ab78547), rabbit anti-TFAM (1:200, Abcam, Catalog #: ab131607). Secondary antibodies were all diluted at 1:500 and include: CF 405 S goat anti-mouse (Biotium, Catalog #: 20830), CF 555 donkey anti-goat (Biotium, Catalog # 20039), CF 555 donkey anti-guinea pig (Biotium, Catalog # 20276), Alexa Fluor 647 donkey anti-goat (Thermo Fisher Scientific, Catalog #: A-21447), CF 647 goat anti-guinea pig (Biotium, Catalog #: 20041), Alexa Fluor 647 goat anti-mouse (Thermo Fisher Scientific, Catalog #: A-21235), Alexa Fluor 647 donkey anti-rabbit (Jackson ImmunoResearch, Catalog #: 711-605-152), Alexa Fluor 647 goat anti-rabbit (Thermo Fisher Scientific, Catalog #: A-21244).

To determine the efficiency of mito-Dendra2 recombination, we quantified the overlap between the endogenous Dendra2 and TOM20 immunostain. For each analyzed cell, we selected 5 bright TOM20 labeled spots that were within the cytoplasm and not part of the mitochondria networks coming from unrecombined cells in the surrounding space while being blinded to the mito-Dendra2 channel. We then qualitatively determined if those spots overlapped with mito-Dendra2 after unblinding the channel.

To determine the mitochondrial content within the oligodendrocyte lineage cells labeled with different cell stage-specific markers, we used the Fiji selection brush tool to trace the soma, nucleus, and a subset of processes from the Z-projections of the targeted cells while being blinded to the mitochondrial channel. Next, we quantified the nucleus and soma area as well as the mean mitochondrial intensity within the traced soma and processes and corrected for background intensity. To determine the percentage of sheaths with mitochondria, we qualitatively determined the presence of 1 or more mitochondrial networks in the analyzed sheaths.

To quantify the presence of TFAM signal in the mitochondria of the oligodendrocyte lineage cells that were stained with stage-specific markers, we performed the analysis on single slices extracted from the Z-stacks. We selected 2-3 regions per cell that included the mitochondria coming from both the soma and processes while being blinded to the TFAM channel. First, we performed thresholding on the mitochondrial channel and used the "Analyze Particles" command in Fiji to automatically generate the ROIs of mitochondria in the selected regions. To eliminate false detection of particles coming from background noise, we filtered out the particles smaller than 0.1 μm^2 in area. Next, we performed thresholding on the TFAM channel and measured the area fraction within the previously determined mitochondrial ROIs to determine what percentage of the area that has mitochondrial signal is covered by TFAM signal in Fiji.

Longitudinal analysis

To observe mitochondrial dynamics occurring with cell fate changes, we performed longitudinal imaging for 20 to 40 consecutive days between P70 to P110. Out of this, data analysis was done for 16 consecutive days for OPCs that differentiated (5 days before, the day of, and 10 days after sheath formation) where day 0 was equivalent to the day when the first sheath/s emerged from the cell. For cells that did not change their fate (remained OPCs or mature oligodendrocytes), data analysis was done for 10 consecutive days out of at least 20-time points where these cells' fate remained unchanged. For cells that died, analysis was done for 10 consecutive days before the cell signal disappeared where the 10^{th} day was the day that apoptotic bodies were detected.

To quantify changes in mitochondrial intensity over time, Z-projections that spanned all the parts of the cell that were to be analyzed were created at each time point. The Z-projections were combined into a hyperstack, registered, and smoothed. ROIs were drawn using the Fiji selection brush tool along the cell soma and 3 primary processes, 3 secondary processes, and 3-4 myelin sheaths (when present) per cell. The cellular compartments were selected independently of the mitochondrial channel and traced over time with reference only to the cytoplasmic channel. At the end of the tracing, they were visually inspected and traced compartments that had overlapping mitochondrial signals coming from neighboring cells were excluded from the ROI. If the same process was not found in all the time points due to cellular morphological changes, it was replaced by tracing a different emerging process of the same branching order from the same cell. The area and mean fluorescence intensity from the mitochondria label were measured within each ROI and the data were normalized to the average mean fluorescence intensity of all the data points analyzed per cell compartment. The average data for all 6 traced processes (3 primaries, 3 secondaries) and 3-4 myelin sheaths per cell were plotted. Mitochondrial circularity in the processes of dying and differentiating OPCs was automatically calculated over time as described above. Calculations were done on Z-projections after thresholding the images and clearing out the mitochondria from the soma, myelin, or other cells in the surroundings.

Electron microscopy dataset analysis

To investigate mitochondrial ultrastructure and determine if mitochondrial differences in the oligodendrocytes and their precursors were present in the human cortex, we used the H01 dataset available online at http://h01-release.storage.googleapis.com/landing.html[39]. The authors of this dataset used a non-pathological temporal lobe sample obtained from a resection surgery of a 45-year-old epileptic patient, sectioned 5000 slices at 30-40 nm thickness, and imaged them using scanning electron microscopy[39]. They also identified the cell types and computationally segmented their structure in 3-D, which can be viewed in Neuroglancer[39]. We used the Volume Annotation and Segmentation Tool (VAST Lite, version 1.4.1)[89] to open the H01 dataset, import the coordinates of our cells of interest taken from Neuroglancer, and fill the cell cytoplasm that had already been automatically segmented. We selected a sample of 5 oligodendrocytes and 5 OPCs and re-confirmed their identity with OPCs having ramified processes, an elongated soma and nucleus, and less heterochromatin than microglia[40] and oligodendrocytes having processes ending on myelin sheaths. We visually inspected and corrected the cytoplasmic fills as needed and analyzed the cell soma and the connected processes separately. Next, we segmented all we could identify as mitochondria in the somas and a subset of processes for each cell type (a total of 26 primary OPC processes and all their branches and a total of 14 primary oligodendrocyte processes and all their branches). We exported the

cytoplasmic and mitochondrial volumes from the region of interest using VAST and calculated mitochondrial volume fraction as the ratio of total mitochondrial volume to total cell compartment volume.

Photoconversion

Photoconversion was done in mito-Dendra2-only labeled cells of 2–3-month-old animals to characterize changes in mitochondrial dynamics in OPCs and mature oligodendrocytes. We referred to changes in mitochondrial shape and content to determine the state of the cell (OPCs: higher content of mixed shape mitochondria distributed along the cell; oligodendrocytes: more mitochondria concentrated on the cell soma and fewer, punctate mitochondria in the proximal processes). Initially, we drew a circular ROI around the soma of the targeted cells. The area within the ROI was then irradiated with a 405 nm laser at 30% power and a speed of 200 Hz and scanned 60 times for a total of 77 seconds using the confocal microscope. Before and after images of the unconverted and photoconverted mito-Dendra2 were captured sequentially using the 488 nm and 552 nm laser wavelengths, respectively. Repeated imaging was done over 4, 24, and 48 hours using consistent image acquisition settings. Image analysis was done using Fiji to follow changes in mitochondrial dynamics over time. The Z-stacks were smoothed, and a circular ROI was drawn around the soma of the targeted cell (replicating the ROI drawn for the photoconversion) on a single slice that showed brightest mito-Dendra2 signal. The same ROI was drawn for all the time points. The mean intensity within the ROI was measured for the unconverted (488 nm) and photoconverted (552 nm) mito-Dendra2 channels. The ratio of the latter to the former was taken for every time point and normalized to the ratio resulting from the time point after photoconversion.

Mitochondrial motility

To determine mitochondrial motility, we tracked the mitochondrial displacement over 30 minutes in awake, anesthetized (isoflurane or ketamine/xylazine), dexmedetomidine hydrochloride, or vehicle-treated animals in acute windows. All images were acquired once a minute on the two-photon microscope from 2–3-month-old and 18-21-month-old animals. For awake imaging, the animals were allowed to adjust to the Mobile HomeCage for 30 minutes before imaging. Similarly, the imaging was done 30 minutes after isoflurane anesthesia (0.8-1%), 15 minutes after intraperitoneal injection of ketamine/xylazine (100 $mgkg^{-1}$/10 $mgkg^{-1}$), 30 minutes after intraperitoneal injection of 0.5 $mgkg^{-1}$ dexmedetomidine hydrochloride (Tocris # 2749) dissolved in distilled water, and 30 minutes after intraperitoneal injection of vehicle. The animal's velocity and locomotion pattern were tracked using the tracking software (version 3.0.0.65 / Beta1) provided with the Neurotar's Mobile HomeCage.

To analyze mitochondrial motility, the time series were blinded, the cells of interest were cropped, and the Z-stacks were corrected for the 3-D drift with reference to the cytoplasmic channel. Z-projections spanning 15 μm were created similarly for each condition, re-corrected for the 3-D drift with reference to the mitochondrial channel, smoothed, and auto-thresholded. The mitochondria coming from other cells, as well as from the soma of the cell of interest were excluded from the analysis. Mitochondria were automatically tracked using the TrackMate[90] (version 7.7.2) plugin in Fiji to determine the displacement of mitochondria tracks and instantaneous velocity. The images were filtered by applying a LoG detector with an estimated object diameter of 3 μm, a quality threshold of 1, and the sub-pixel localization was checked. The Simple LAP Tracker was applied with a linking max distance of 3 μm, gap-closing max distance of 3 μm, and max frame gap of 2. The tracks with less than 5 spots were excluded and post-hoc visual inspection was done to correct for major errors in particle tracking.

Next, to address any remaining drift coming from the live imaging, we corrected the mitochondrial displacement values via two methods. Method 1 consisted of first detecting the most stable mitochondrial track within the analyzed cells, which corresponded to the track that traveled the smallest distance within the 30 minutes. We assumed that any displacement recorded for the most stable track was due to image drift and not true mitochondrial motility. Then we subtracted the displacement of this track from the corresponding displacement values of all the other mitochondrial tracks in the image. After this correction, we compiled all the mitochondrial displacement values coming from 18 OPCs (1015 mitochondria tracks) and 16 oligodendrocytes (100 mitochondria tracks) in the awake conditions (Fig. 8e) and analyzed the data distribution. We defined the sum of the mean and the standard deviation from the data (2.4 μm) to be the displacement threshold and any tracks displacing 2.4 μm or more were considered motile. To independently correct for image motion artifacts, we employed a second correction method. This consisted of running the same steps on TrackMate for the cytoplasmic channel as we did for the mitochondrial channel with the only difference being the defined object diameter, which was adjusted accordingly to focus the object on the soma of the cell as the most stable compartment. It was made sure that the same cytoplasmic spot was tracked for every paired condition. Next, every mitochondrial displacement value was corrected for the cytoplasmic displacement value coming from the corresponding cell.

Statistical analysis

All statistical analyses were performed using GraphPad Prism (version 9.5.1) or Excel. Each dot represents a cell, the lines/traces are at the mean and the error bars represent the s.e.m. Normal distribution and equal variance were assumed but not formally tested for all the datasets and sample numbers were determined based on previous publications[74,78]. Statistical tests were kept consistent throughout the study and one-way ANOVA with Tukey's multiple comparisons test was used for comparisons between three groups and unpaired or paired t-tests were used for comparisons between two groups, unless specified otherwise. Animals were randomly assigned to each experimental group. The cells analyzed throughout the study were selected solely based on the quality of the images and the ability to distinguish individual cells and cell compartments. The cells analyzed for the mitochondrial motility experiments were randomly selected with reference only to the first time point of the time series. The cells analyzed from the EM dataset were selected only based on what best satisfied the identification criteria for the cell types analyzed. Data was blinded for each condition of mitochondrial motility analysis (awake, isoflurane, ketamine/xylazine, dexmedetomidine hydrochloride, vehicle) and animal age when analyzing mitochondrial length and distribution in young and aged animals. Throughout the study, when defining ROIs of the cell compartments, the analyzer was blinded to the mitochondrial channel and referred only to the cytoplasmic channel to prevent any bias on the regions selected. No animals were excluded from the statistical analysis.

Reporting summary

Further information on research design is available in the Nature Portfolio Reporting Summary linked to this article.

Data availability

All the analyzed data are represented within the manuscript and all the other data are available from the authors upon unrestricted request. Source data are provided with this paper.

References

1. Simons, M. & Nave, K.-A. Oligodendrocytes: Myelination and Axonal Support. *Cold Spring Harb. Perspect. Biol.* **8**, a020479 (2016).
2. Stadelmann, C., Timmler, S., Barrantes-Freer, A. & Simons, M. Myelin in the Central Nervous System: Structure, Function, and Pathology. *Physiol. Rev.* **99**, 1381–1431 (2019).

3. Young, K. M. et al. Oligodendrocyte dynamics in the healthy adult CNS: evidence for myelin remodeling. *Neuron* **77**, 873–885 (2013).
4. Hill, R. A., Li, A. M. & Grutzendler, J. Lifelong cortical myelin plasticity and age-related degeneration in the live mammalian brain. *Nat. Neurosci.* **21**, 683–695 (2018).
5. Kessaris, N. et al. Competing waves of oligodendrocytes in the forebrain and postnatal elimination of an embryonic lineage. *Nat. Neurosci.* **9**, 173–179 (2006).
6. Zhu, X. et al. Age-dependent fate and lineage restriction of single NG2 cells. *Development* **138**, 745–753 (2011).
7. Dimou, L., Simon, C., Kirchhoff, F., Takebayashi, H. & Götz, M. Progeny of Olig2-expressing progenitors in the gray and white matter of the adult mouse cerebral cortex. *J. Neurosci.* **28**, 10434–10442 (2008).
8. Barres, B. A. & Raff, M. C. Proliferation of oligodendrocyte precursor cells depends on electrical activity in axons. *Nature* **361**, 258–260 (1993).
9. Calver, A. R. et al. Oligodendrocyte population dynamics and the role of PDGF in vivo. *Neuron* **20**, 869–882 (1998).
10. Hill, R. A., Patel, K. D., Goncalves, C. M., Grutzendler, J. & Nishiyama, A. Modulation of oligodendrocyte generation during a critical temporal window after NG2 cell division. *Nat. Neurosci.* **17**, 1518–1527 (2014).
11. Bechler, M. E., Byrne, L. & Ffrench-Constant, C. CNS myelin sheath lengths are an intrinsic property of oligodendrocytes. *Curr. Biol.* **25**, 2411–2416 (2015).
12. Mitew, S. et al. Pharmacogenetic stimulation of neuronal activity increases myelination in an axon-specific manner. *Nat. Commun.* **9**, 306 (2018).
13. Xin, W. & Chan, J. R. Myelin plasticity: sculpting circuits in learning and memory. *Nat. Rev. Neurosci.* **21**, 682–694 (2020).
14. Hill, R. A., Nishiyama, A. & Hughes, E. G. Features, Fates, and Functions of Oligodendrocyte Precursor Cells. *Cold Spring Harb. Perspect. Biol.* **16**, a041425 (2024).
15. Bahat, A. & Gross, A. Mitochondrial plasticity in cell fate regulation. *J. Biol. Chem.* **294**, 13852–13863 (2019).
16. Pernas, L. & Scorrano, L. Mito-Morphosis: Mitochondrial Fusion, Fission, and Cristae Remodeling as Key Mediators of Cellular Function. *Annu. Rev. Physiol.* **78**, 505–531 (2016).
17. Chen, H. & Chan, D. C. Mitochondrial Dynamics in Regulating the Unique Phenotypes of Cancer and Stem Cells. *Cell Metab.* **26**, 39–48 (2017).
18. Khacho, M. et al. Mitochondrial Dynamics Impacts Stem Cell Identity and Fate Decisions by Regulating a Nuclear Transcriptional Program. *Cell Stem Cell* **19**, 232–247 (2016).
19. Esteban-Martínez, L. et al. Programmed mitophagy is essential for the glycolytic switch during cell differentiation. *EMBO J.* **36**, 1688–1706 (2017).
20. Iwata, R., Casimir, P. & Vanderhaeghen, P. Mitochondrial dynamics in postmitotic cells regulate neurogenesis. *Science* **369**, 858–862 (2020).
21. Zehnder, T. et al. Mitochondrial biogenesis in developing astrocytes regulates astrocyte maturation and synapse formation. *Cell Rep.* **35**, 108952 (2021).
22. Baum, T. & Gama, V. Dynamic properties of mitochondria during human corticogenesis. *Development* **148**, dev194183 (2021).
23. Tait, S. W. G. & Green, D. R. Mitochondrial Regulation of Cell Death. *Cold Spring Harb. Perspect. Biol.* **5**, a008706 (2013).
24. Márquez-Jurado, S. et al. Mitochondrial levels determine variability in cell death by modulating apoptotic gene expression. *Nat. Commun.* **9**, 389 (2018).
25. Schoenfeld, R. et al. Oligodendroglial differentiation induces mitochondrial genes and inhibition of mitochondrial function represses oligodendroglial differentiation. *Mitochondrion* **10**, 143–150 (2010).
26. Zhang, Y. et al. An RNA-Sequencing Transcriptome and Splicing Database of Glia, Neurons, and Vascular Cells of the Cerebral Cortex. *J. Neurosci.* **34**, 11929–11947 (2014).
27. Meyer, N. & Rinholm, J. E. Mitochondria in Myelinating Oligodendrocytes: Slow and Out of Breath? *Metabolites* **11**, 359 (2021).
28. Yazdankhah, M. et al. BNIP3L-mediated mitophagy is required for mitochondrial remodeling during the differentiation of optic nerve oligodendrocytes. *Autophagy* **17**, 3140–3159 (2021).
29. Sun, L. O. et al. Spatiotemporal Control of CNS Myelination by Oligodendrocyte Programmed Cell Death through the TFEB-PUMA Axis. *Cell* **175**, 1811–1826.e21 (2018).
30. Gil, M. & Gama, V. Emerging mitochondrial-mediated mechanisms involved in oligodendrocyte development. *J. Neurosci. Res* **101**, 354–366 (2023).
31. Rinholm, J. E. et al. Movement and structure of mitochondria in oligodendrocytes and their myelin sheaths. *Glia* **64**, 810–825 (2016).
32. Nakamura, D. S. et al. Mitochondrial dynamics and bioenergetics regulated by netrin-1 in oligodendrocytes. *Glia* **69**, 392–412 (2021).
33. Grimm, A. & Eckert, A. Brain aging and neurodegeneration: from a mitochondrial point of view. *J. Neurochem* **143**, 418–431 (2017).
34. Chan, D. C. Mitochondrial Dynamics and Its Involvement in Disease. *Annu. Rev. Pathol.: Mechanisms Dis.* **15**, 235–259 (2020).
35. Neumann, B. et al. Metformin Restores CNS Remyelination Capacity by Rejuvenating Aged Stem Cells. *Cell Stem Cell* **25**, 473–485.e8 (2019).
36. Schain, A. J., Hill, R. A. & Grutzendler, J. Label-free in vivo imaging of myelinated axons in health and disease with spectral confocal reflectance microscopy. *Nat. Med* **20**, 443–449 (2014).
37. Hill, R. A. & Grutzendler, J. Uncovering the biology of myelin with optical imaging of the live brain. *Glia* **67**, 2008–2019 (2019).
38. Chapman, T. W., Olveda, G. E., Bame, X., Pereira, E. & Hill, R. A. Oligodendrocyte death initiates synchronous remyelination to restore cortical myelin patterns in mice. *Nat. Neurosci.* **26**, 555–569 (2023).
39. Shapson-Coe, A. et al. A petavoxel fragment of human cerebral cortex reconstructed at nanoscale resolution. *Science* **384**, eadk4858 (2024).
40. Buchanan, J. et al. Oligodendrocyte precursor cells ingest axons in the mouse neocortex. *Proc. Natl Acad. Sci.* **119**, e2202580119 (2022).
41. Campbell, C. T., Kolesar, J. E. & Kaufman, B. A. Mitochondrial transcription factor A regulates mitochondrial transcription initiation, DNA packaging, and genome copy number. *Biochim. et. Biophys. Acta (BBA) - Gene Regulat. Mech.* **1819**, 921–929 (2012).
42. McCarron, J. G. et al. From Structure to Function: Mitochondrial Morphology, Motion and Shaping in Vascular Smooth Muscle. *J. Vasc. Res* **50**, 357–371 (2013).
43. Yu, S. B. & Pekkurnaz, G. Mechanisms Orchestrating Mitochondrial Dynamics for Energy Homeostasis. *J. Mol. Biol.* **430**, 3922–3941 (2018).
44. Misgeld, T. & Schwarz, T. L. Mitostasis in neurons: Maintaining mitochondria in an extended cellular architecture. *Neuron* **96**, 651–666 (2017).
45. Schulz, H. Beta oxidation of fatty acids. *Biochim. et. Biophys. Acta (BBA) - Lipids Lipid Metab.* **1081**, 109–120 (1991).
46. Harris, J. J. & Attwell, D. The Energetics of CNS White Matter. *J. Neurosci.* **32**, 356–371 (2012).
47. Bizzozero, O. A., Sanchez, P. & Tetzloff, S. U. Effect of ATP depletion on the palmitoylation of myelin proteolipid protein in young and adult rats. *J. Neurochem* **72**, 2610–2616 (1999).
48. Viader, A. et al. Aberrant Schwann Cell Lipid Metabolism Linked to Mitochondrial Deficits Leads to Axon Degeneration and Neuropathy. *Neuron* **77**, 886–898 (2013).

49. Toyama, B. H. et al. Identification of long-lived proteins reveals exceptional stability of essential cellular structures. *Cell* **154**, 971–982 (2013).
50. Kassmann, C. M. et al. A role for myelin-associated peroxisomes in maintaining paranodal loops and axonal integrity. *FEBS Lett.* **585**, 2205–2211 (2011).
51. Kirischuk, S., Neuhaus, J., Verkhratsky, A. & Kettenmann, H. Preferential localization of active mitochondria in process tips of immature retinal oligodendrocytes. *NeuroReport* **6**, 737–741 (1995).
52. Ashrafi, G. & Schwarz, T. L. The pathways of mitophagy for quality control and clearance of mitochondria. *Cell Death Differ.* **20**, 31–42 (2013).
53. Hirabayashi, Y. et al. Most axonal mitochondria in cortical pyramidal neurons lack mitochondrial DNA and consume ATP. *bioRxiv* 2024.02.12.579972 https://doi.org/10.1101/2024.02.12.579972 (2024).
54. Xu, Y. K. T., Call, C. L., Sulam, J. & Bergles, D. E. Automated in vivo Tracking of Cortical Oligodendrocytes. *Front Cell Neurosci.* **15**, 667595 (2021).
55. Chapman, T. W., Kamen, Y., Piedra, E. T. & Hill, R. A. Oligodendrocyte Maturation Alters the Cell Death Mechanisms That Cause Demyelination. *J. Neurosci.* **44**, e1794232024 (2024).
56. Kim, S. Y. et al. Neuronal mitochondrial morphology is significantly affected by both fixative and oxygen level during perfusion. *Front Mol. Neurosci.* **15**, 1042616 (2022).
57. Hinton, A. et al. A Comprehensive Approach to Sample Preparation for Electron Microscopy and the Assessment of Mitochondrial Morphology in Tissue and Cultured Cells. *Adv. Biol. (Weinh.)* **7**, e2200202 (2023).
58. Rone, M. B. et al. Oligodendrogliopathy in Multiple Sclerosis: Low Glycolytic Metabolic Rate Promotes Oligodendrocyte Survival. *J. Neurosci.* **36**, 4698–4707 (2016).
59. Rao, V. T. S. et al. Distinct age and differentiation-state dependent metabolic profiles of oligodendrocytes under optimal and stress conditions. *PLoS One* **12**, e0182372 (2017).
60. Funfschilling, U. et al. Glycolytic oligodendrocytes maintain myelin and long-term axonal integrity. *Nature* **485**, 517–521 (2012).
61. Morland, C., Henjum, S., Iversen, E. G., Skrede, K. K. & Hassel, B. Evidence for a higher glycolytic than oxidative metabolic activity in white matter of rat brain. *Neurochem. Int.* **50**, 703–709 (2007).
62. Tondera, D. et al. SLP-2 is required for stress-induced mitochondrial hyperfusion. *EMBO J.* **28**, 1589–1600 (2009).
63. Yao, C.-H. et al. Mitochondrial fusion supports increased oxidative phosphorylation during cell proliferation. *eLife* **8**, e41351 (2019).
64. Zhou, W. et al. HIF1α induced switch from bivalent to exclusively glycolytic metabolism during ESC-to-EpiSC/hESC transition. *EMBO J.* **31**, 2103–2116 (2012).
65. Haak, L. L., Grimaldi, M. & Russell, J. T. Mitochondria in myelinating cells: calcium signaling in oligodendrocyte precursor cells. *Cell Calcium* **28**, 297–306 (2000).
66. Battefeld, A., Popovic, M. A., de Vries, S. I. & Kole, M. H. P. High-Frequency Microdomain Ca2+ Transients and Waves during Early Myelin Internode Remodeling. *Cell Rep.* **26**, 182–191.e5 (2019).
67. French, H. M., Reid, M., Mamontov, P., Simmons, R. A. & Grinspan, J. B. Oxidative Stress Disrupts Oligodendrocyte Maturation. *J. Neurosci. Res* **87**, 3076–3087 (2009).
68. Lewis, T. L., Turi, G. F., Kwon, S.-K., Losonczy, A. & Polleux, F. Progressive decrease of mitochondrial motility during maturation of cortical axons in vitro and in vivo. *Curr. Biol.* **26**, 2602–2608 (2016).
69. Faits, M. C., Zhang, C., Soto, F. & Kerschensteiner, D. Dendritic mitochondria reach stable positions during circuit development. *eLife* **5**, e11583 (2016).
70. Zhou, B. et al. Facilitation of axon regeneration by enhancing mitochondrial transport and rescuing energy deficits. *J. Cell Biol.* **214**, 103–119 (2016).
71. Nakamura, D. S., Gothié, J.-D. M., Kornfeld, S. F., Kothary, R. & Kennedy, T. E. Expression and subcellular localization of mitochondrial docking protein, syntaphilin, in oligodendrocytes and CNS myelin sheath. *Glia* https://doi.org/10.1002/glia.24425 (2023).
72. Smit-Rigter, L. et al. Mitochondrial Dynamics in Visual Cortex Are Limited In Vivo and Not Affected by Axonal Structural Plasticity. *Curr. Biol.* **26**, 2609–2616 (2016).
73. Jackson, J. G., O'Donnell, J. C., Takano, H., Coulter, D. A. & Robinson, M. B. Neuronal Activity and Glutamate Uptake Decrease Mitochondrial Mobility in Astrocytes and Position Mitochondria Near Glutamate Transporters. *J. Neurosci.* **34**, 1613–1624 (2014).
74. Agarwal, A. et al. Transient Opening of the Mitochondrial Permeability Transition Pore Induces Microdomain Calcium Transients in Astrocyte Processes. *Neuron* **93**, 587–605.e7 (2017).
75. Lu, T.-Y. et al. Norepinephrine modulates calcium dynamics in cortical oligodendrocyte precursor cells promoting proliferation during arousal in mice. *Nat. Neurosci.* **26**, 1739–1750 (2023).
76. Fiore, F. et al. Norepinephrine regulates calcium signals and fate of oligodendrocyte precursor cells in the mouse cerebral cortex. *Nat. Commun.* **14**, 8122 (2023).
77. Paukert, M. et al. Norepinephrine controls astroglial responsiveness to local circuit activity. *Neuron* **82**, 1263–1270 (2014).
78. Umpierre, A. D. et al. Microglial calcium signaling is attuned to neuronal activity in awake mice. *eLife* **9**, e56502 (2020).
79. Khorchid, A., Cui, Q., Molina-Holgado, E. & Almazan, G. Developmental regulation of α1A-adrenoceptor function in rat brain oligodendrocyte cultures. *Neuropharmacology* **42**, 685–696 (2002).
80. Chalmers, S., Saunter, C. D., Girkin, J. M. & McCarron, J. G. Age decreases mitochondrial motility and increases mitochondrial size in vascular smooth muscle. *J. Physiol.* **594**, 4283–4295 (2016).
81. Takihara, Y. et al. In vivo imaging of axonal transport of mitochondria in the diseased and aged mammalian CNS. *Proc. Natl Acad. Sci. USA* **112**, 10515–10520 (2015).
82. Spitzer, S. O. et al. Oligodendrocyte Progenitor Cells Become Regionally Diverse and Heterogeneous with Age. *Neuron* **101**, 459 (2019).
83. Madisen, L. et al. A robust and high-throughput Cre reporting and characterization system for the whole mouse brain. *Nat. Neurosci.* **13**, 133–140 (2010).
84. Pham, A. H., McCaffery, J. M. & Chan, D. C. Mouse lines with photo-activatable mitochondria to study mitochondrial dynamics. *Genesis* **50**, 833–843 (2012).
85. Hill, R. A., Damisah, E. C., Chen, F., Kwan, A. C. & Grutzendler, J. Targeted two-photon chemical apoptotic ablation of defined cell types in vivo. *Nat. Commun.* **8**, 15837 (2017).
86. Arshadi, C., Günther, U., Eddison, M., Harrington, K. I. S. & Ferreira, T. A. SNT: a unifying toolbox for quantification of neuronal anatomy. *Nat. Methods* **18**, 374–377 (2021).
87. Longair, M. H., Baker, D. A. & Armstrong, J. D. Simple Neurite Tracer: open source software for reconstruction, visualization and analysis of neuronal processes. *Bioinformatics* **27**, 2453–2454 (2011).
88. Ferreira, T. A. et al. Neuronal morphometry directly from bitmap images. *Nat. Methods* **11**, 982–984 (2014).
89. Berger, D. R., Seung, H. S. & Lichtman, J. W. VAST (Volume Annotation and Segmentation Tool): Efficient Manual and Semi-Automatic Labeling of Large 3D Image Stacks. *Front. Neural Circuits* **12**, 88 (2018).
90. Ershov, D. et al. TrackMate 7: integrating state-of-the-art segmentation algorithms into tracking pipelines. *Nat. Methods* **19**, 829–832 (2022).

Acknowledgements

We thank members of the Hill and Hoppa laboratories at Dartmouth College for valuable feedback on this work. We would also like to thank Dr. Shahroz Khan for helping with data analysis, Matthew Ciolkowski for

assistance with immunohistochemistry, and Dr. Henry Higgs for sharing the TOM20 antibody. This study was supported by National Institutes of Health grant no. R01NS122800 and the Esther A. & Joseph Klingenstein Fund and Simons Foundation to R.A.H. and American Heart Association grant no. 23PRE1018862, https://doi.org/10.58275/AHA.23PRE1018862.pc.gr.161154 to Xh.B.

Author contributions

Xh.B. and R.A.H. designed and performed all the experiments, analyzed the data, wrote the manuscript, and secured funding. R.A.H. supervised the study.

Competing interests

The authors declare no competing interest.

Additional information

Supplementary information The online version contains supplementary material available at https://doi.org/10.1038/s41467-024-51016-2.

Correspondence and requests for materials should be addressed to Robert A. Hill.

Peer review information *Nature Communications* thanks Xianshu Bai and the other anonymous reviewer(s) for their contribution to the peer review of this work. A peer review file is available.